Master of Science Thesis

An Investigation of the Non-Linear 3D Flow Effects Relevant for Leading Edge Inflatable Kites

Michael Deaves

September 1st, 2015

Faculty of Aerospace Engineering · Delft University of Technology
Department of Wind Energy · Technical University of Denmark

An Investigation of the Non-Linear 3D Flow Effects Relevant for Leading Edge Inflatable Kites

Master of Science Thesis

by

Michael Deaves

In partial fulfillment of the requirements for the degree of

Master of Science
in Aerospace Engineering
at the Delft University of Technology

&

Master of Science
in Engineering in Wind Energy
at the Technical University of Denmark

within the **European Wind Energy Master - EWEM**
Rotor Design track (Aerodynamics)

September 1st, 2015

Faculty of Aerospace Engineering · Delft University of Technology
Department of Wind Energy · Technical University of Denmark

"I am an enthusiast, but not a crank in the sense that I have some pet theories as to the proper construction of a flying machine. I wish to avail myself of all that is already known and then if possible add my mite to help on the future worker who will attain final success."

Wilbur Wright (1899)

Delft University Of Technology Faculty Of Aerospace Engineering
and
Technical University of Denmark Department Of Wind Energy

The undersigned hereby certify that they have read and recommend to the Delft University of Technology Faculty of Aerospace Engineering and the Technical University of Denmark Department of Wind Energy for acceptance a thesis entitled **"An Investigation of the Non-Linear 3D Flow Effects Relevant for Leading Edge Inflatable Kites"** by **Michael Deaves** in partial fulfillment of the requirements for the degree of **Master of Science**.

Dated: September 1st, 2015

Supervisor: ______________________
Dr. Roland Schmehl

Supervisor: ______________________
Dr. Mac Gaunaa

Reader: ______________________
Dr. Wim Bierbooms

Reader: ______________________
Ir. Thijs Gillebaart

Summary

The kite power group at TU Delft is currently researching the use of leading edge inflatable (LEI) kites for use in power generation. A thorough understanding of the aeroelastics of these kites is paramount to the development of system simulation models and optimum kite and system designs. The current lack of understanding is therefore seen as a roadblock to the development of a commercially viable kite power system.

The aeroelastics of LEI kites are complicated by three main challenges.

- There is a high degree of coupling between the flexible kite and the aerodynamic loading. This means that a fluid-structure interaction approach is typically needed to produce accurate simulation results.
- The low aspect ratio and large anhedral of the kite means that 3D effects are significant [57].
- During normal power production it is desirable to fly the kite at high angles of attack where significant non-linear viscous phenomena (e.g. flow seperation) are known to occur [45].

In order to model correctly the 3D viscous aerodynamic phenomena present in LEI kite flight a computational approach utilizing a steady-state Reynolds-Average-Navier-Stokes (RANS) solver has been suggested. This work presents a review of relevant literature, outlines the computational approach taken, and discusses the limitations and computational costs of the approach.

It was found that the RANS approach is able to model the kite's flow environment up to angles of attack of 24°. At angles larger than this significant flow separation from the suction surface of the kite precludes the use of a steady-state solver. At angles as low as 18° significant non-linear effects begin to take effect, decreasing lift and increasing drag. It was also found that at lower angles of attack separation from behind the leading edge tube serves to decrease effective camber and therefore lift. The computational cost of the approach is heavily influenced by the quality of the mesh generated, in particular the presence of non-orthogonal cells.

It is concluded that the RANS approach is capable of quantifying well the non-linear flow effects of LEI kites at moderately high angles of attack. The challenge of this method in the future will be to decrease it's significant computational costs so that it may be used in the context of systems modeling, optimization, or fluid-structure interaction.

Acknowledgements

This thesis represents the culmination of over two years of intense study and personal growth. I would not be at the point I am now without the incredible help and support I have received from those around me as well as those back home in Canada.

Firstly I would like to thank my co-supervisor Prof. Roland Schmehl for his enthusiasm and excitement surrounding the topic of kite power. His passion for the subject has affected everyone within the kite power group, and in my opinion is the only reason this research area exists at all. I would also like to thank my co-supervisor Mac Gaunaa for his ongoing patience and encouragement.

A special thanks goes out to Rachel Leuthold for supplying a constant source of good energy and raw vegetables, and for being an empathetic sounding board during times of frustration. A big thank you to Ye Zhang and Thijs Gillebaart for providing me numerous hours of OpenFOAM and Pointwise expertise. Dave Aberdeen too deserves my praises for his hard work with the SurfPlan software package. Also my gratitude belongs to the Enevate team of Christophe Grete, Johannes Peschel, Christian Friedrich, Anastasios Tzavellas, Felix Friedl, Pietro Faggiani, and Lukas Brown. These men have managed to impart to me more knowledge about kite power, and engineering in general, than any course or text book ever could. Of course this section would not be complete without acknowledging all the other EWEM students. It is because of all of you that these last two years have been among the best of my entire life.

At last I would like to thank those closest to me. Heleen, whose support during the last year has been unwavering. Finally my parents for providing me with this great opportunity along with the sense and character needed to make something of it.

Delft, The Netherlands — Michael Deaves
September 1st, 2015

Contents

List of Figures

List of Tables

Nomenclature

Latin Symbols

A	Characteristic Area	$[m^2]$
AR	Aspect Ratio	$[-]$
a	3D Lift Curve Slope	$[-]$
a_1	Turbulence Model Constant	$[-]$
B_L	Sail Equation Coefficient	$[-]$
b	Flattened Kite Wing Span or LEI Airfoil Camber	$[m]$
C_D	3D Drag Coefficient	$[-]$
C_d	2D Drag Coefficient	$[-]$
C_f	Skin Friction Coefficient	$[-]$
C_L	3D Lift Coefficient	$[-]$
C_l	2D Lift Coefficient	$[-]$
C_M	3D Moment Coefficient	$[-]$
C_m	2D Moment Coefficient	$[-]$
C_p	Pressure Coefficient	$[-]$
C_x	x-Direction Force Coefficient	$[-]$
C_y	y-Direction Force Coefficient	$[-]$
$C_{D,eff}$	Effective 3D Drag Coefficient	$[-]$
$C_{D,L=0}$	3D Drag Coefficient at Zero Lift	$[-]$
$C_{D,min}$	Minimum 3D Drag Coefficient	$[-]$
$C_{D,p}$	Parasitic Drag Coefficient	$[-]$
$CD_{k\omega}$	Turbulence Model Limiter	$[-]$

c	Airfoil Chord	$[m]$
c_{avg}	Average Chord	$[m]$
c_{mid}	Mid-Span Chord	$[m]$
$\mathbf{D}$	Drag Force Vector	$[kgm/s^2]$
d	LEI Airfoil Thickness or Distance to Nearest Wall	$[m]$
e	Span Efficiency Factor	$[-]$
$\mathbf{F}_t$	Traction Force Vector	$[kgm/s^2]$
F_1	Shear Stress Transport Smoothing Parameter	$[-]$
F_2	Shear Stress Transport Smoothing Parameter	$[-]$
K	Turbulent Eddy Diffusivity	$[m]$
k	Turbulent Kinetic Energy	$[m^2/s^2]$
$\mathbf{L}$	Lift Force Vector	$[kgm/s^2]$
l_l	Geometric Length Scale	$[m]$
Ma	Mach Number	$[-]$
N	Number of Grid Points	$[-]$
N_t	Number of Time Steps	$[-]$
P	Kinetic Energy Production	$[kg/ms^3]$
P_M^{max}	Maximum Mechanical Power	$[kgm^2/s^3]$
Pe	Pecelt Number	$[-]$
p	Pressure	$[kg/ms^2]$
Re	Reynolds Number	$[-]$
S_{ij}	Mean Strain Rate Tensor	$[1/s]$
Sc_t	Turbulent Schmidt Number	$[-]$
t	LEI Airfoil Relative Thickness or Time	$[-]$ or $[s]$
t_l	Large Eddie Turnover Time	$[s]$
U_∞	Free Stream Flow Velocity	$[m/s]$
u	Flow Velocity	$[m/s]$
u^*	Friction Velocity	$[m/s]$
u_l	Characteristic Eddy Velocity	$[m/s]$
$\mathbf{v}_a$	Apparent Wind Velocity Vector	$[m/s]$
$\mathbf{v}_t$	Tether Reel Out Velocity Vector	$[m/s]$
$\mathbf{v}_w$	Wind Velocity Vector	$[m/s]$
$\mathbf{v}_{k,\tau}$	Kite Tangential Velocity Vector	$[m/s]$
v	Kolmogorov Velocity Scale	$[m/s]$
W_{ij}	Vorticity Tensor	$[1/s]$
x, y, z	The Three Spatial Dimensions	$[m]$
y^+	Non-Dimensional Wall Units	$[-]$

Greek Symbols

α	Angle of Attack	$[deg]$
$\alpha_{L=0}$	Zero-Lift Angle of Attack	$[deg]$
β	Turbulence Model Constant	$[-]$
β^*	Turbulence Model Constant	$[-]$
γ	Turbulence Model Constant	$[-]$
Δs	First Boundary Layer Cell Height	$[m]$
Δt	Time Step	$[s]$
δ_{ij}	Kronecker Delta	$[-]$
ϵ	Turbulent Dissipation Rate	$[m^2/s^3]$
ϵ_L	Sail Excess Length	$[-]$
η	Kolmogorov Length Scale	$[m]$
κ	LEI Airfoil Relative Camber or von Karman Constant	$[-]$
μ	Dynamic Viscosity	$[kg/ms]$
μ_t	Turbulent Dynamic Viscosity	$[kg/ms]$
ν	Kinematic Viscosity	$[m^2/s]$
ν_t	Turbulent Kinematic Viscosity	$[m^2/s]$
ρ	Air Density	$[kg/m^3]$
σ_k	Turbulence Model Constant	$[-]$
σ_ω	Turbulence Model Constant	$[-]$
τ	Kolmogorov Time Scale	$[s]$
τ_w	Wall Shear Stress	$[kg/ms^2]$
τ_{ij}	Reynolds Stress Tensor	$[kg/ms^2]$
ϕ	Example Turbulence Model Parameter or Example Flow Variable	$[-]$
Ω	Vorticity Magnitude	$[1/s]$
ω	Specific Turbulent Dissipation Rate	$[1/s]$

Abbreviations

AWE	Airborne Wind Energy
CD	Central Differencing
CFD	Computational Fluid Dynamics
CPU	Computer Processing Unit
DNS	Direct Numerical Simulation
DOF	Degrees of Freedom
EWEM	European Wind Energy Master
FSI	Fluid-Structure Interaction

FVM	Finite Volume Method
HAWT	Horizontal Axis Wind Turbine
KCU	Kite Control Unit
LEI	Leading Edge Inflatable
LLT	Lifting Line Theory
NACA	National Advisory Committee for Aeronautics
NS	Navier-Stokes
RANS	Reynolds-Average-Navier-Stokes
RHS	Right Hand Side
SIMPLE	Semi-Implicit Method for Pressure Linked Equations
SST	Shear Stress Transport
UD	Upwind Differencing
VLM	Vortex Lattice Method

Chapter 1

Introduction

1.1 Airborne Wind Energy

Over the past few years a community of scientific and commercial institutions have been developing what could turn out to be the next paradigm of wind energy technology. Known collectively as Airborne Wind Energy (AWE), these technologies possess a number of advantages over horizontal axis wind turbines (HAWT), making it possible that they may come to supplant HAWTs and become the dominant wind energy technology in years to come.

1.1.1 Concepts and Advantages

The AWE community is currently evaluating many different concepts. A great overview of these concepts is provided by Cherubini et. al. [12]. Many of the most successful concepts share the characteristic feature of a tethered aerodynamic surface (wing or kite), flying fast cross-wind motions to extract energy from the wind. These cross-wind concepts can be further divided into groups depending on the type of wing used and where in the system electricity is generated.

Rigid Wing vs. Soft Wing Rigid wing concepts use composite materials to construct an aerodynamic structure similar to a small airplane or a glider. Soft wing concepts borrow from the kite and paragliding industries and use specially designed fabric kites. Rigid wing concepts enjoy greater aerodynamic efficiencies but typically at larger costs per square meter of wing surface. Safety is also of greater concern for rigid wing designs.

Ground Based vs. Airborne Generators Ground based concepts rely on the strong pulling force from the tether to turn a drum connected to a generator placed on the ground. These concepts must eventually reel back in when the maximum tether length is reached. For this reason they are also known as 'yo-yo' concepts. Airborne generating concepts use

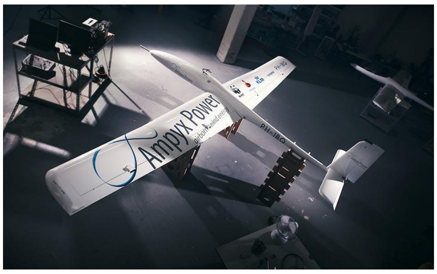

(a) Ampyx Power's rigid wing system.

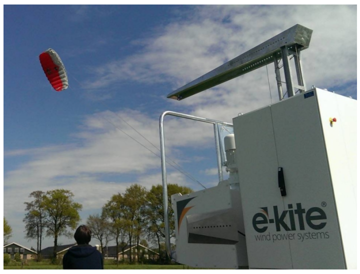

(b) e-kite's flexible ram-air wing.

Figure 1.1: Examples of a rigid wing and a soft wing.

(a) EnerKite's ground based generator.

(b) Makani Power's wing mounted turbines.

Figure 1.2: Examples of ground based generation and airborne generation.

small wind turbines attached to the wing to generate electricity in the air. This power is sent through an electrically conductive tether to the ground.

Cross-wind concepts have many advantages over conventional HAWTs. They have the potential to access the stronger, less intermittent winds at higher altitudes. They are more mobile than HAWTs, allowing them to be deployed in a variety of short term or remote scenarios. Due to their concentration of mass close to the ground they could be more suited to floating offshore applications. Finally, they have the potential to utilize significantly less material in their construction, reducing the cost of the electricity generated. Figure 1.3 shows a comparison between a cross-wind AWE concept and a conventional HAWT. Due to the increase in swept area with radius the outer 30% of a conventional wind turbine blade is responsible for over half of the energy production [16]. In the cross-wind concept the functions of the tower and inner part of the blade are replaced by the light weight tether and kite control system.

All of these advantages are currently driving the AWE community to develop an economically viable commercial scale system. It is unclear at the present moment which concept will be the first to reach commercial viability.

1.2 TU Delft's Cross-Wind Kite Power System

The Kite Power group at TU Delft is actively involved in the research and development of a cross-wind AWE system. The current concept utilizes a 20 kW ground based generator connected by a single tether to a flexible 25 m^2 Leading Edge Inflatable (LEI) kite.

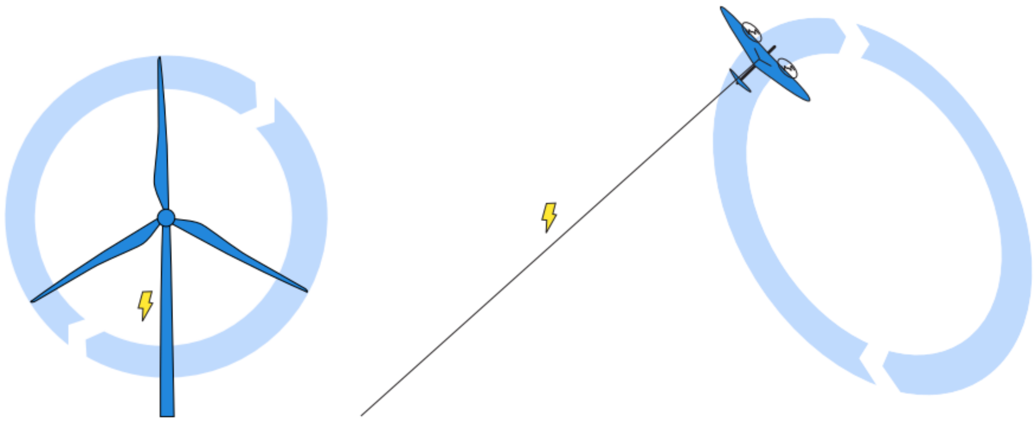

Figure 1.3: A comparison of a conventional HAWT and the kite power concept. Figure is illustrated by R. Paelinck, and reproduced from [16].

Hanging below the kite is a remotely controlled Kite Control Unit (KCU) that provides the steering and depower actuation through the kite's bridle lines. The kite and KCU can be seen in Figure 1.4.

Figure 1.4: TU Delft's LEI kite and KCU.

The kite power system utilizes pumping power cycles to generate electricity. These cycles consist of two main phases. During the reel out phase the kite flies fast cross-wind figure eight manoeuvres in order to increase the relative velocity of the kite with respect to the air [7]. The large traction force generated is used to turn an electrical generator on the ground producing positive electrical energy. Once the maximum tether length is reached, the KCU alters the kite's bridle geometry, reducing the traction force, and allowing the kite to be pulled back in with a minimal expenditure of energy. These pumping cycles then repeat. For a more in depth description of the kite power system concept the reader is referred to the Airborne Wind Energy text released in 2013 [16].

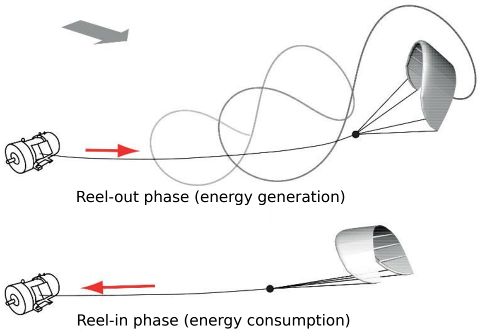

(a) One complete pumping cycle.

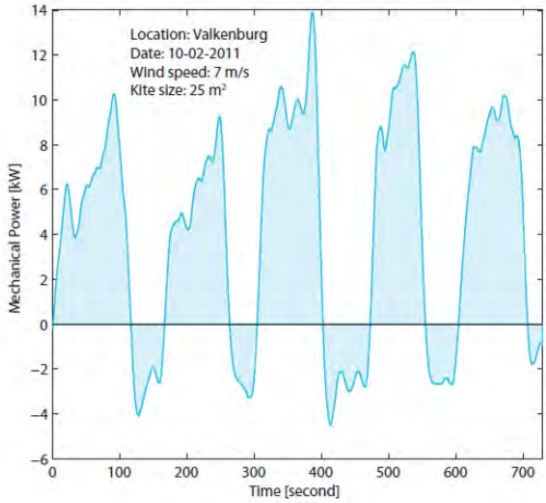

(b) Power production during many pumping cycles.

Figure 1.5: TU Delft's kite power system operation reproduced from [45].

1.2.1 Cross-Wind Power Operating Principal

Both [37] and [2] have produced thorough theoretical analyses of the cross-wind power concept's main operating principal. The key results are discussed here briefly, but for a more in depth analysis the reader is refereed to their publications.

Figure 1.6 shows the flow velocities and lift and drag forces of a kite flying horizontally, directly down wind with high tangential velocity $\mathbf{v}_{k,\tau}$. The wind velocity, tether reel out velocity, and resulting apparent wind velocity are shown as $\mathbf{v}_w$, $\mathbf{v}_t$, and $\mathbf{v}_a$ respectively. Also shown are the resulting lift, drag, and tether (traction) forces, $\mathbf{L}$, $\mathbf{D}$, and $\mathbf{F}_t$ respectively.

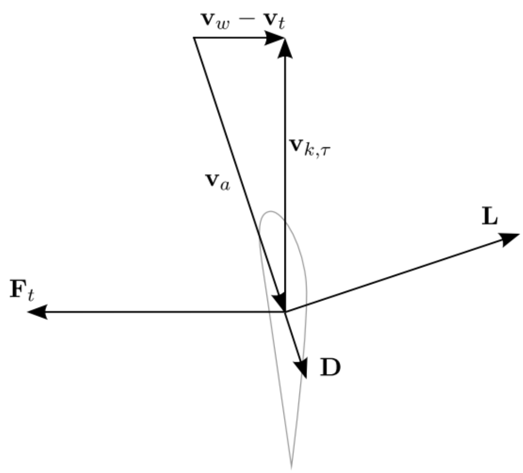

Figure 1.6: A simplified analysis of the forces and flow velocities on a kite in crosswind motion.

The operating principal of the kite is seen clearly from this simplified case. It is the tangential component of the lift that pulls the kite forward with high crosswind velocities. The radial component of the lift is responsible for the large tether force and as a result the considerable power generating capabilities of the system. In turn the drag of the kite balances the tangential component of the lift force such that there is a limit on the maximum crosswind velocity that can be attained. It is shown by both [37] and [2] that in the case of a massless kite and by considering only the aerodynamic forces on the wing the maximum mechanical power is generated at a reel out velocity of $\mathrm{v}_t = \frac{1}{3}\mathrm{v}_w$. Under these assumptions the maximum mechanical power that can be produced is given by Equation 1.1.

$$P_M^{max} = \frac{2}{27}\rho A \mathrm{v}_w^3 \left(\frac{C_L^3}{C_{D,eff}^2} \right) \tag{1.1}$$

Where ρ is the density of the air, A is the characteristic area of the kite, v_w unperturbed wind speed, C_L is the kite lift coefficient and $C_{D,eff}$ is the effective drag coefficient of the kite that accounts for the parasitic drag of lines and bridle systems.

In reality the maximum power that can be generated from the kite is a much more complicated optimization problem since a number of important factors have been left out of this analysis. Tether elevation angle, wind shear, kite depower capabilities and many other factors have been ignored. A more thorough discussion can be found in [18]. Never the less this simplified analysis stresses the importance of an aerodynamically efficient kite that maximizes its value of $\left(\frac{C_L^3}{C_{D,eff}^2} \right)$. This fact is important as it leads to kites operating near stall conditions as discussed in section 2.2.

1.3 Thesis Direction

Of critical importance in the development of TU Delft's kite power system is a thorough understanding of the complex and highly non-linear aeroelastic phenomena that occur during LEI kite flight. This understanding would allow for the development of more efficient kite designs and an accurate simulation environment that could be used to improve the system design and optimization process. Unfortunately the aeroelastics of LEI kite flight are complicated by three main challenges.

- There is a high degree of coupling between the flexible kite and the aerodynamic loading. This means that a fluid-structure interaction (FSI) approach is typically needed to produce accurate simulation results.
- The low aspect ratio and large anhedral of the kite means that 3D effects are significant [57].
- During normal power production it is desirable to fly the kite at high angles of attack where significant non-linear viscous phenomena (e.g. flow seperation) are known to occur [45].

Due to these challenges there is currently a large gap in the literature with respect to understanding the aeroelastics of LEI kite flight. Recent advances in the field of Computational Fluid Dynamics (CFD), specifically Reynolds-Average-Navier-Stokes (RANS) methods, may enable the investigation of two of the three main challenges listed above. It is the purpose of this thesis to discover how RANS methods could be used to investigate the 3D, nonlinear effects present in LEI kite flows. Specifically the following questions will be answered.

- To what extent are RANS methods able to model the 3D non-linear effects (i.e. flow separation) present?
- What are the tools and best practices that should be used when applying these methods?
- How sensitive are the results to changes in the various simulation parameters?
- What is their computational cost and how might this be reduced while maintaining solution accuracy?
- How might these methods be used in an FSI context?

Chapter 2

LEI Kite Aeroelastics

2.1 Kite Geometry

The kite power group currently uses a $25\,\mathrm{m}^2$ leading edge inflatable kite known as the TUD-25mV2, or simply the V2. The inflated leading edge strut provides the kite with some rigidity, while a bridle system restricts the kite shape and transmits the aerodynamic loads to the tether. The kite is divided spanwise into 8 sections. Seven inflated struts positioned along the span stretch from the leading edge to the trailing edge and provide further structural rigidity. Figure 2.1 shows a 3D model of the kite in the kite design software SurfPlan™. Figure 1.4 shows a photo of the kite, bridle lines, and KCU while in flight.

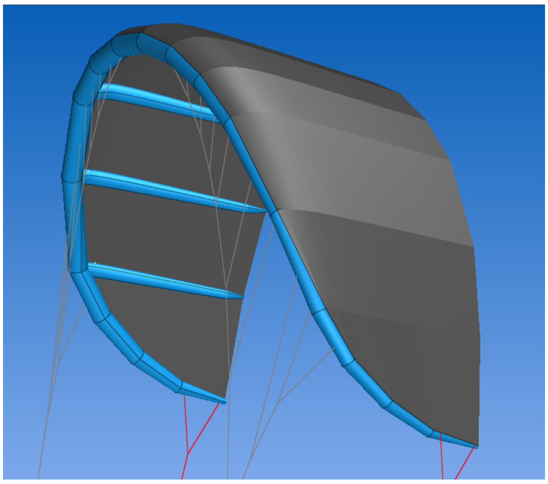

Figure 2.1: A 3D model of the TUD-25mV2 LEI kite in SurfPlan™.

The kite has a flattened wing span of $b = 11.7\,\mathrm{m}$, a mid-span chord of $c_{mid} = 2.72\,\mathrm{m}$, and an average chord of $c_{avg} = 2.13\,\mathrm{m}$. The chord reduces to zero at the tips. The kite's flattened area is $A = 25\,\mathrm{m}^2$ and its flattened aspect ratio is $AR = 5.3$ defined as

$AR = \frac{b^2}{A}$. In all cases the mid-span chord and the flattened area will be used as the kite's characteristic length and area respectively.

2.2 Flight Envelope

The TU Delft kite power system currently operates at a height of no more than 700 m above the ground, although discussions are under way to increase the flight ceiling to 1 km in order to increase power capture. Figure 2.2 shows some representative altitude and apparent velocity data gathered during a test in June 2012.

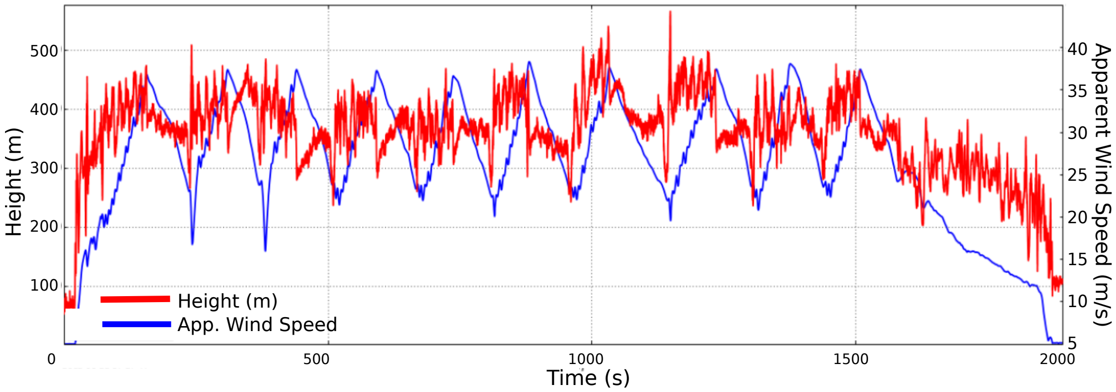

Figure 2.2: Representative kite altitude and apparent wind velocity during several pumping cycles.

During normal operation the kite altitude is bounded between 150 m and 500 m with apparent flow velocities ranging from 20 m/s to 45 m/s. Using the kite's mid-span chord as a characteristic length the kite's operating Reynolds numbers vary between Re $= 3.75\,\mathrm{x}10^6$ and Re $= 8.44\,\mathrm{x}10^6$.

Ruppert has collected the best available data relating to angle of attack and side slip angle [45]. Some issues with respect to this data are discussed in section 5.3. Figure 2.3 shows that the angle of attack seen by the kite during the traction phase varies between 20° and 50° with a mean value of approximately 30°. At such large angles of attack significant flow separation is expected to occur along the suction surface of the kite. In addition, flow separation is expected to occur behind the leading edge tube.

The side slip angle that the kite sees further complicates its aeroelastic behavior. The side slip angle varies between −15° and +15° regularly during the traction phase depending on whether it is performing the right-hand or the left-hand turn in the flight path.

2.3 Fluid-Structure Interaction

The LEI kite problem is challenging because there is a strong coupling between the kites structural dynamics and the airflow over the kite. The kite shape influences the pressure distribution across the surface of the kite, and in turn the flow pressure determines the

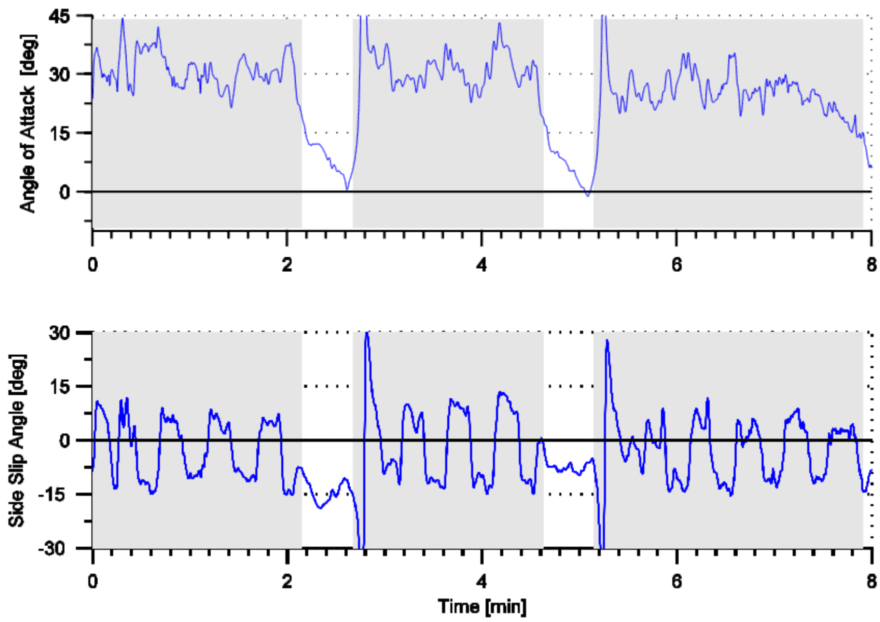

Figure 2.3: Typical angle of attack α and side slip angle β during power production reproduced from [45].

kite shape. In general these two components must be modeled together. This section introduces the current state of the art in modeling the complex FSI problem of LEI kites.

2.3.1 Partioned vs. Monolithic Solvers

FSI solvers can be divided broadly into two categories. Partitioned solvers and monolithic solvers [17]. The differences between the two categories can be seen in Figure 2.4.

Monolithic solvers attempt to model the entire aeroelastic behavior in one system of equations that is solved simultaneously. Partitioned solvers separate the flow problem from the structural problem into two systems of equations that are solved at different times. Partitioned solvers therefore need a method to pass pressure and shear stress information to the structural solver, and a method for passing structural deformation data to the flow solver. Some examples of monolithic solvers that have been applied to membrane flows can be seen in [5] and [3]. Good examples of partitioned FSI solvers applied to LEI kite flows are [7] and [8].

Monolithic solvers tend to be more stable and don't suffer from as many numerical issues relating to the coupling of the structure with the flow solver. Partitioned solvers on the other hand enjoy the advantage of modularity. Many different aerodynamic models can be coupled with the same structural model and vice versa. This modularity makes the development of effective FSI tools much easier since it is not known a priori which models will work the best in any given circumstance. The kite power group at TU Delft has adopted the partitioned solver approach for their FSI modelling of LEI kite aeroelasticity.

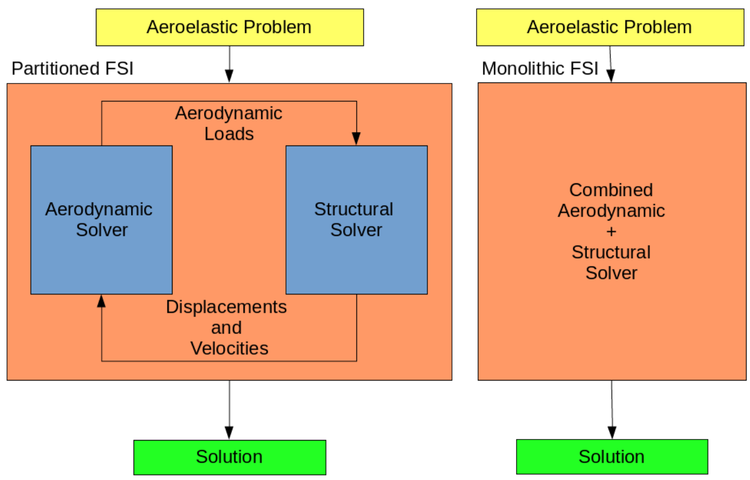

Figure 2.4: The conceptual differences between monolithic and partitioned FSI solvers.

2.4 Kite Structural Models

There are many LEI kite structural models that are currently under development. Each model can be evaluated on its fidelity, that is how well it reproduces the structural behavior of a real LEI kite, and its computational cost. In general models with higher numbers of degrees of freedom provide higher fidelity and higher computational costs, although this is not necessarily so. Figure 2.5 and Figure 2.6 show a comparison of the available LEI kite structural models.

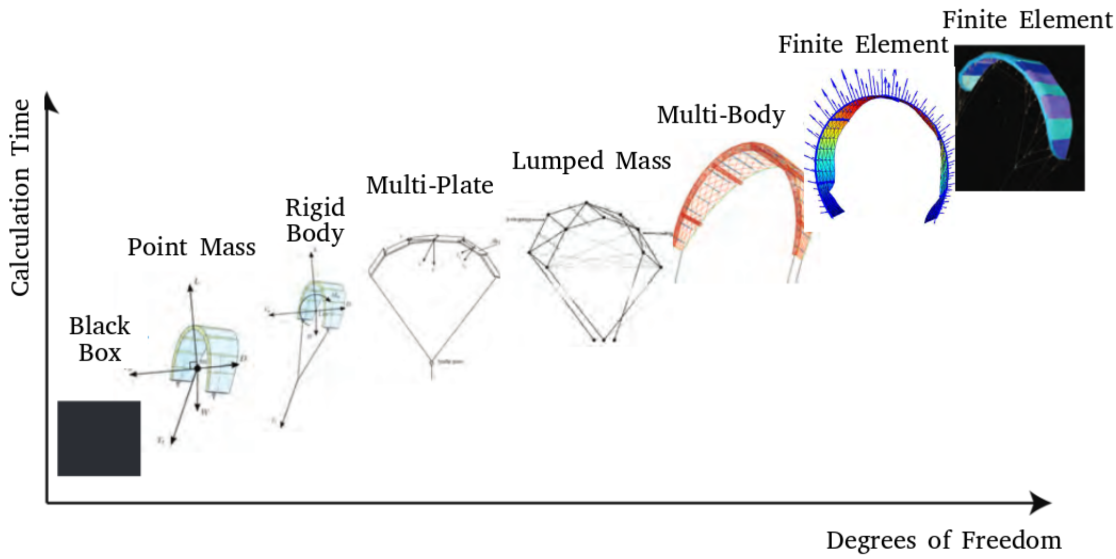

Figure 2.5: Comparison of the available LEI kite structural models. Reproduced from [7].

In addition to the models shown above a non-linear canopy FEM model is currently under development by J. Berens [6] for the purposes of fundamental FSI investigations in the

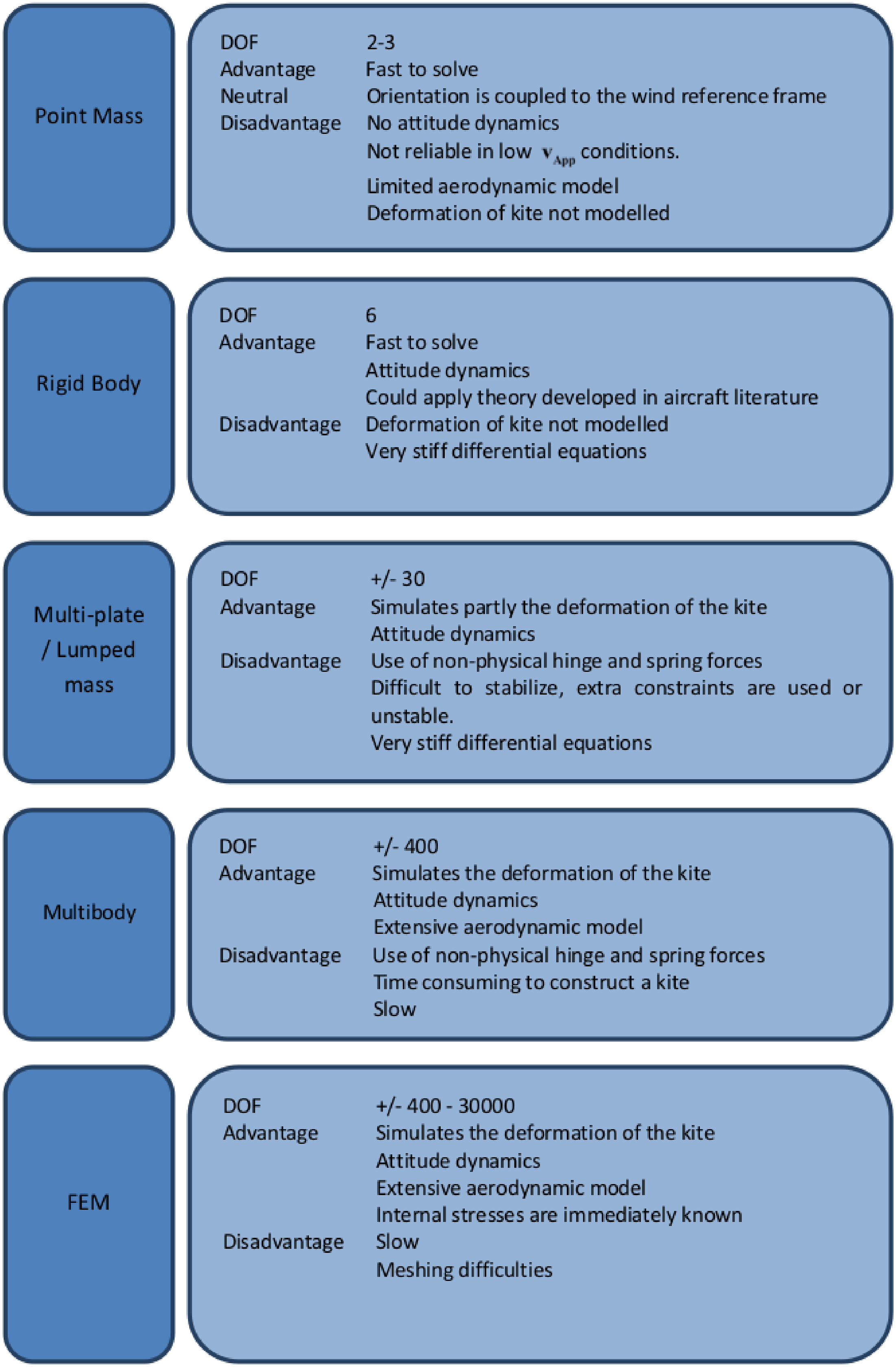

Figure 2.6: Details of the available LEI kite structural models. Reproduced from [45].

near future. For a thorough evaluation of these models with respect to LEI kite FSI problems the reader is referred to [45] and [7].

2.5 Aerodynamic Models

There exists little literature concerning the flow over an LEI kite. However, membrane flows have been studied extensively in relation to natural systems such as bat wings and veined leaves, canvas structures such as tents and convertible car roofs, micro-UAVs, sail-bladed wind turbines, yacht sails, and ram air wings. The most literature exists for yacht sails and ram air wings. These systems also share some very similar flow conditions to LEI kites used in power generation. Large angles of attack, frequent flow separation, high coupling between the fluid and structure, and a high degree of three dimensionality in the flow are all also present in LEI kite flows. An review of the literature on these subjects is presented below.

2.5.1 Black Box Model

The simplest aerodynamic model applied to a power producing kite was used by [19]. The model divides the kite into 3 main surfaces, one large horizontal lifting surface, and two vertical control surfaces used for steering the kite. Empirically determined lookup tables are then created to relate the state of the kite with the lift and drag produced on each kite surface. The model is able to model kite performance with reasonable results, however the lift and drag values used have little reflection upon reality. In addition since the lift and drag values have to be determined empirically to bring the model into alignment with experimental results this method can not be used during the design stage.

2.5.2 2D Finite-Strip Approximation

In this method cross sectional airfoil performance is predicted beforehand, usually by inviscid flow solvers such as XFOIL, and then the entire 3D wing is modelled as a collection of 2D 'finite strips' that behave as if they had infinite span. Using this model 3D effects like tip recirculation, cross-flow, and lift induced drag, are not captured accurately. [41] performed a study on using 2D strip theory to predict performance of two-lobed parawings and found that the method also had issue predicting separation at high angles of attack.

2.5.3 Breukels Aerodynamic Model

The model currently in use with the TU Delft kite power group was developed by J. Breukels [8]. It was designed to give reasonable results and analytical flexibility with minimal computation cost. The model takes the finite strip approach a step further and incorporates the effect of membrane deformations. The kite is divided in the spanwise direction into a number of 2D cross sections. As in the 2D finite-strip model each cross section is assumed to act on the flow as if it were infinitely long and placed into perfectly aligned flow. The lift, drag and moment of each cross-section is provided from a look-up table from the values of angle af attack, α, relative airfoil thickness, $t = d/c$, and relative airfoil camber, $\kappa = b/c$, which in turn are related to the structural deformations of the kite. These values are provided by RANS or XFOIL simulations before hand.

$$C_l = f(\kappa, t, \alpha) \qquad C_d = f(\kappa, t, \alpha) \qquad C_m = f(\kappa, t, \alpha) \tag{2.1}$$

A schematic of the cross-section is shown in Figure 2.7.

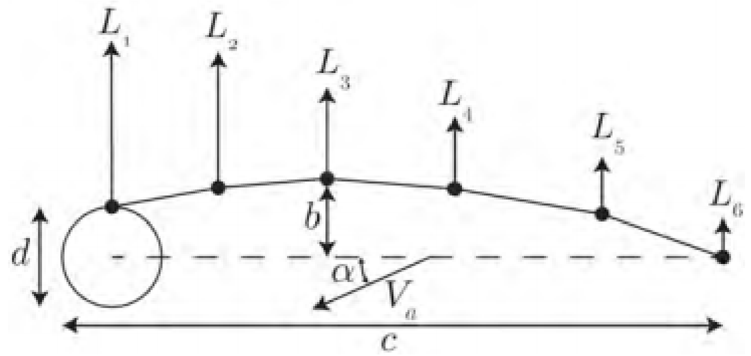

Figure 2.7: Cross sectional view of Breukel's simplified airfoil cross section. Reproduced from [8].

The integral aerodynamic forces are then distributed to 6 nodes of the airfoil cross-section by use of a series of weighting functions. Unfortunately the selection of these weighting functions is considered somewhat arbitrary since 6 values of the function have to be determined (the force on each node), but only one moment equation is available. The system is thus underdetermined.

Bosch has pointed out a number of functional criticisms with Breukels' model [7].

- Increasing the camber does not always increase the drag force.
- As a results of the 2D finite-strip approximation spanwise velocity components are ignored. In such a low aspect ratio, highly curved wing as an LEI kite this assumption is certainly questionable.
- When local node velocities are included in the angle of attack calculation the model becomes unstable.
- The 2D RANS results produced are questionable in themselves due to the large angles of attack (up to 20°) used and the inability of most CFD codes to capture large flow separations.
- The definitions of camber and thickness used produce some peculiarities since the leading edge tube diameter couples both together. As a result the model may overemphasize the importance of certain variable interactions.

Breukels did try to correct for 3D effects by using a linear vortex-lattice code. He assumes that the relationship between lift curve slope and anhedral angle is independent of airfoil shape. Although as pointed out by [52] this method has its own drawbacks including the assumptions of linear (attached) flow, and the use of a different kite's lift curve slope for the analysis of the current LEI kite.

2.5.4 Potential Flow Methods

For an in depth description of the subtle differences between the potential flow methods available the reader is referred to [35] or the great low speed aerodynamics textbook [29].

Flow past 2D inextensible flexible membranes was first conducted in the context of planar sails. Inviscid, irrotational, thin airfoil theory was combined with static equilibrium considerations by Thwaites [50], Nielsen [43], Voelz [55], and Greenhalgh [24] in order to yield the so called *sail equation* shown in Equation 2.2.

$$C_L \approx 2\pi\alpha + B_L\sqrt{\epsilon_L} \tag{2.2}$$

Where $\epsilon_L = (l - c)/c$ is known as the sail excess length, where l is the sail length and c is the airfoil chord.

Depending on the numerical technique used to solve the integrals involved slightly varying results were found. Thwaits found $B_L = 0.636$, Nielsen found $B_L = 0.728$, and Greenhalgh found $B_L = 0.70$.

Inviscid potential flow methods were also used by [23], [36], [20], [34] to model the flow around yacht sails. Since these methods are computationally inexpensive they are still commonly used in the design and analysis of yacht sails. It is common for the pure potential flow technique to be modified slightly to account for the effects of viscosity. [23] used 3D lifting line theory (LLT) combined with 2D RANS simulations of the sail cross sections to account for non-linear flow effects. The Helmholtz thick wake model was used by [36] to account for the effects of flow separation in 2D. This is coupled to a static equilibrium structural model of the sail to converge to the sail's steady state loaded shape. A 3D free wake vortex lattice method (VLM) was combined with a boundary layer integral formulation by [20] to correct for the effects of viscosity. A coupled 2D vortex sheet method was used by [34] along with a non-linear membrane model of the sail to investigate the unsteady dynamics of the sail. While many of these methods look promising, they often encounter problems with large amount of flow separation, and over predict lift and under predict drag at high angles of attack.

Much like yacht sails, potential flow methods have been used to model ram air kites with some success. A VLM flow solver has been coupled with a non-linear finite element representation of a ram air kite by [11] and [10]. In this approach the flow is assumed to remain attached throughout.

Work by [22] and [9] proposed a computationally efficient method for determining aerodynamic performance of kites (LEI or ram air) and compared the results to 3D RANS simulations of a simplified kite geometry, shown in Figure 2.9. Also [52] investigated the feasibility of using this aerodynamic model in FSI simulations of LEI kites. The method

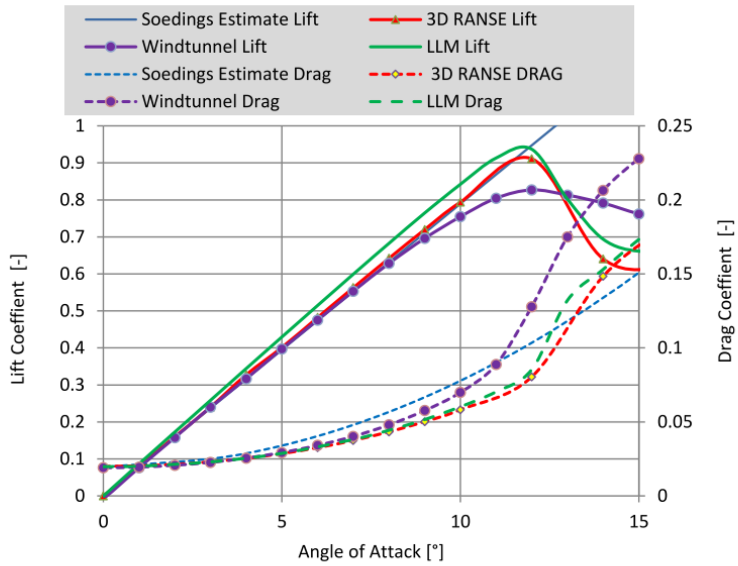

Figure 2.8: Accuracy of Graf's non-linear LLT method compared to 3D RANS simulations and wind tunnel data for an upwind yacht sail. Reproduced from [23].

is based on the iterative coupling between a VLM and 2D sectional airfoil coefficients. The results obtained are excellent as long as the flow stays attached. However, like many other modified potential flow methods, it has problems dealing with stalled flow.

2.5.5 Navier-Stokes Methods

In order to capture the effects of flow separation it is often needed to result to solving the viscous Navier-Stokes equations. The details of how this is done are covered in more depth in section 3.1.

A numerical analysis of 2D flexible membrane sails using the Navier-Stokes equations as the fluid model is presented in [47], in the hopes of capturing the effects of viscosity. The results were in agreement with the analytical results of the *sail equation*, Equation 2.2, for certain limiting cases where the effects of viscosity were minimal. Due to limited computational resources the flows analyzed were assumed to be laminar, which is certainly not the case for an LEI kite.

Work by [48] presents an analysis of viscous, turbulent, flexible membrane computations and compares them with classical sail theory. The authors used a 2D discretization to solve the RANS equations at a realistic Reynolds numbers of $1.3\,\text{x}10^6$. The k-ω Shear Stress Transport (SST) [42] equations are used to model the turbulence and close the system. They are compared to earlier results by the same authors computed using the k-ϵ turbulence model. It was found that the k-ϵ model was unable to predict leading edge separation, while the k-ω SST model was, at least ostensibly, able to do so. It was found, however, that when compared to the available experimental data the k-ω SST model over predicts the lift.

Work by [13] employed the use of the commercial CFD package FLUENT in the analysis

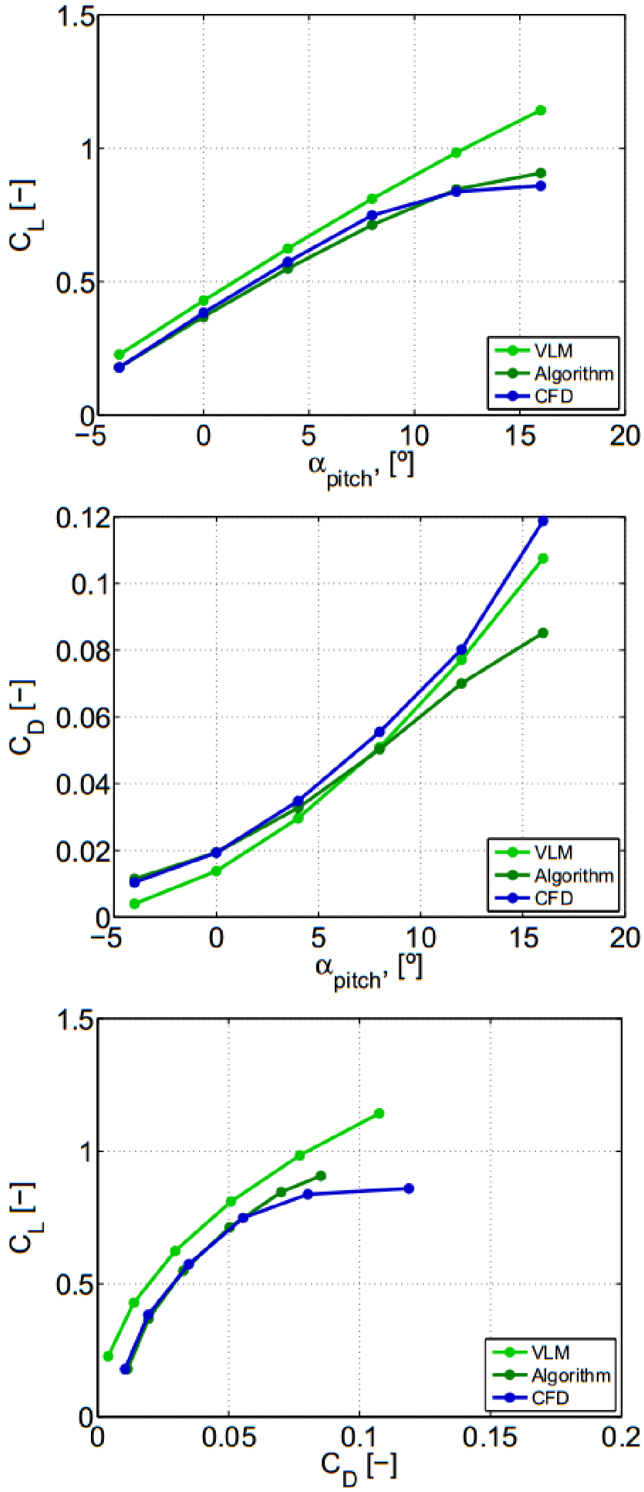

Figure 2.9: Comparison of lift and drag coefficients from the reference kite using the standard VLM, Gaunaa's viscous corrected VLM, and 3D RANS calculations. Reproduced from [22].

of upwind sail performance. Since no experimental data was available to the authors they bench marked the available turbulence models against the canonical backward facing step problem. The realizable k-ϵ model was shown to be the most accurate.

Work by [54] is the first to validate RANS simulations of upwind yacht sails with actual wind tunnel measurements. The agreement is surprisingly good, even for separated flows as shown in Figure 2.10 and Figure 2.11. Both leading edge and trailing edge separation were present in the flows investigated. Following the same reasoning as [48] the k-ω SST turbulence model was used because of its ability to model strong adverse pressure gradients and separation.

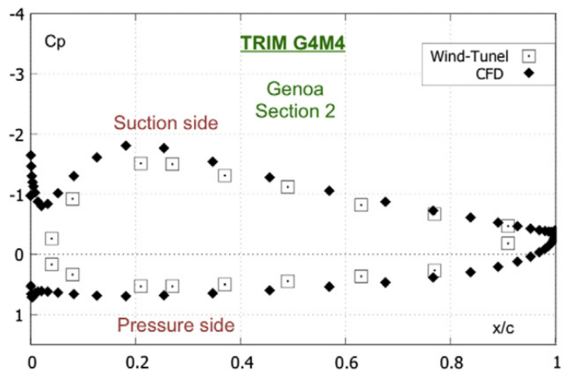

Figure 2.10: Wind tunnel measurements compared with 3D RANS results on an upwind yacht sail. Reproduced from [54].

2.5.6 Experimental Results

Some experimental results for ram air kites are available in the literature. A Flexfoil Blade III foil kite was flown behind a moving vehicle by [14], and the tether force and angle measurements were used to produce estimates of aerodynamic performance. The author also developed a 3D flow model based on LLT that was incorporated into a dynamic model of the kite system. Results of the 3D lifting line model were compared to 3D RANS results of a Clark Y sectioned kite geometry simplification from [38] and it was found that in the linear region of well attached flow good agreement is found. However, much like the attempts at modelling sail flow past yacht sails, at larger angles of attack the LLT model cannot reproduce the flow separation present.

Wok by [15] placed a ram air kite in the wind tunnel and used photogrammetry and laser scanning to record its loaded 3D shape. Then 3D RANS simulations were performed on the found geometry to determine the aerodynamic performance of the wing. The k-ω SST turbulence model was used as well as a transition flow model. A number of wind tunnel experiments were conducted by [4] with the goal of decreasing drag on paraglider (ram air) wings. Another series of wind tunnel experiments on 2D parafoil sections were conducted by [21]. Unfortunately due to the differences in geometry between ram air kites and LEI kites these experimental results can at best be used as an order of magnitude check against any LEI kite simulations.

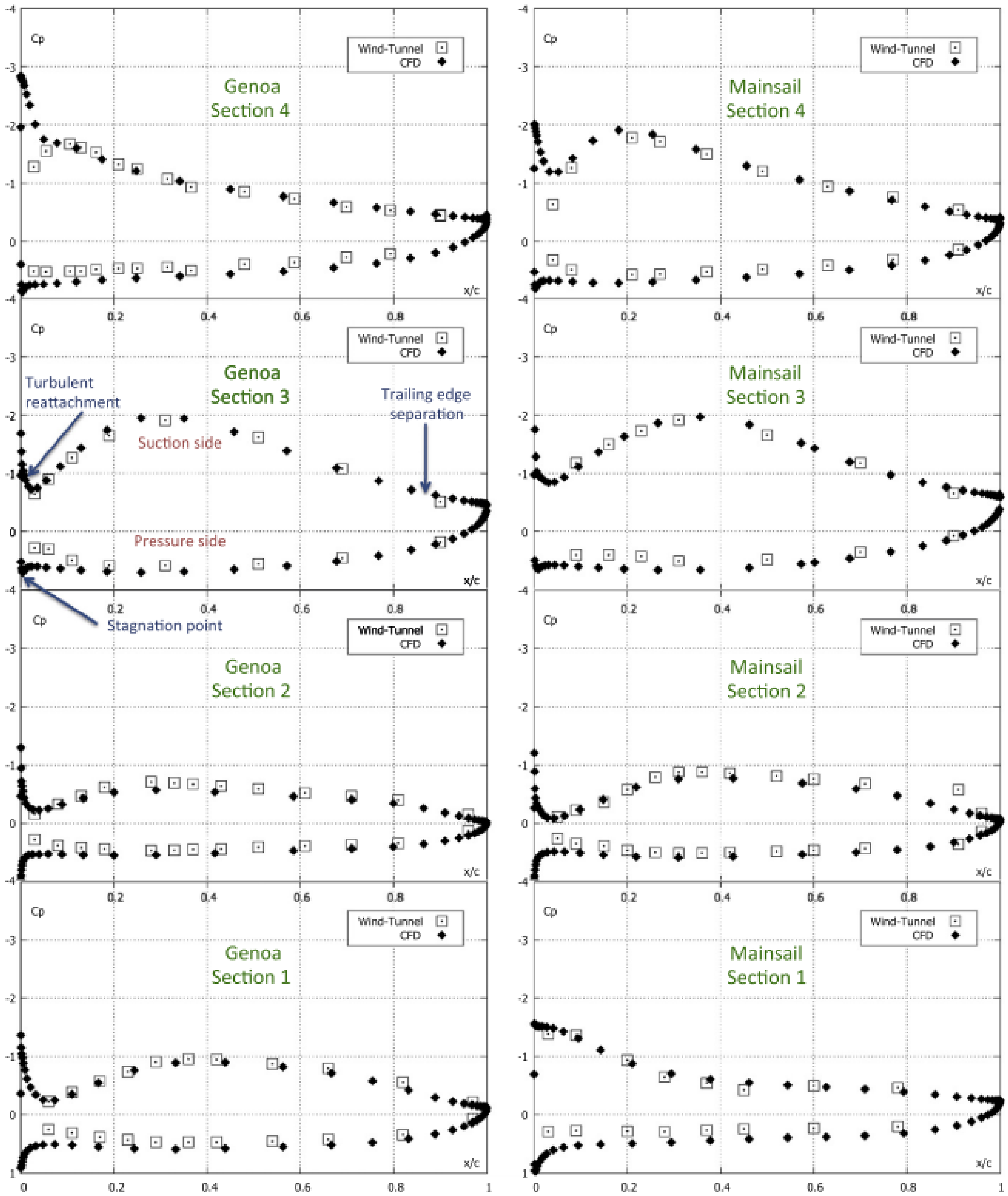

Figure 2.11: Wind tunnel measurements compared with 3D RANS results on an upwind yacht sail. Reproduced from [54].

2.6 The Problem of 3D Viscous Flows

From the available literature of upwind sail and ram air kite flow modeling it is clear that 2D finite strip approximations, or potential flow methods are unable to model effectively the phenomenon of flow separation. As discussed in section 2.2 angles of attack of the kite in flight can be quite large. At these angles flow separation from the suction surface of the kite is expected to occur, precluding these models from use.

Based on the work of [54], in which 3D RANS methods were validated against wind tunnel experiments for the case of mild flow separation, it would seem that RANS methods are the best choice of aerodynamic model for separated LEI kite flows. For this reason these methods were explored further in this work.

Unfortunately RANS methods are too computationally expensive to be coupled with a structural model of the kite of a similar level of accuracy. As such it was decided that this work will focus solely on the aerodynamic analyses of LEI kites by assuming a kite shape *a priori*. This shape will not be determined from a structural solver, but instead from the kite design software SurfPlan™. Only in this way can the aerodynamic investigations that are needed be completed in the allotted time and with the resources available.

Chapter 3

Methods

3.1 Computational Fluid Dynamics

The physics of incompressible (low mach number), Newtonian flows at constant temperature, like those found in LEI kite problems, are described by the Navier-Stokes (NS) and continuity equations. These equations represent mathematically the concepts of conservation of momentum and conservation of mass respectively. They are shown in Einstein summation notation in Equation 3.1 and Equation 3.2.

$$\frac{\partial u_i}{\partial t} + u_j \frac{\partial u_i}{\partial x_j} = -\frac{1}{\rho}\frac{\partial p}{\partial x_i} + \nu \frac{\partial^2 u_i}{\partial x_j \partial x_j} \tag{3.1}$$

$$\frac{\partial u_i}{\partial x_i} = 0 \tag{3.2}$$

Here x_i represents the three spatial dimensions x, y, and z. u_i represents the three velocity components, u_x, u_y, and u_z. p is the pressure, and ρ and ν are the fluid density and kinematic viscosity respectively. Together the momentum and continuity equations form a non-linear system of partial differential equations, and are as such notoriously difficult to solve. CFD is the branch of fluid mechanics that aims to use computers to find numerical solutions to governing flow equations like the NS equations.

3.1.1 Potential Flow Methods

As described in section 2.5 many of the methods used to analyze flows similar to those found in LEI kites resort to assumptions about the flow in order to simplify the governing equations. The most popular methods are so called *potential flow* methods, which make the assumptions of zero-viscosity, and irrotationality of the flow. This serves to linearize the NS equations making them much easier to solve numerically. For high Reynolds number attached flows, where the effects of viscosity and flow rotationality are confined to a thin boundary layer surrounding the body, they model the flow physics rather well.

Unfortunately for the flows involved with LEI kites the assumptions of zero-viscosity and irrotationality are poor simplifications since many important flow phenomena are caused by and intricately linked to the effects of viscosity and vorticity. Most notably flow separation is not captured by potential flow methods but plays an important role in LEI kite aerodynamics.

3.1.2 Finite Volume Methods

The Finite-Volume-Method (FVM) an increasingly popular technique used to solve the NS equations numerically. In the FVM the flow domain is discretized into a number of small cells, known as a mesh. The flow variables (velocity, pressure, etc.) are assumed to be constant within each cell. The derivatives present in the NS equations are then approximated numerically for a solution to the NS equations. As the flow mesh is refined, the solution should approach the actual flow solution. An example of a flow mesh used with the FVM can be seen in Figure 3.3.

Solving the NS equations as shown in Equation 3.1 and Equation 3.2 numerically is known as Direct Numerical Simulation (DNS). Although this technique can be used for Reynolds numbers in the low thousands, the mesh resolution needed to resolve the turbulent fluctuations of higher Reynolds number flows makes DNS infeasible for most common engineering problems (including LEI kites).

3.1.3 Turbulent Scales

In the 1940's Kolmogorov developed the universal equilibrium theory to describe the behavior of turbulent flows [30] [31]. By assuming scale separation, that is that the dynamics of the smallest scales are statistically independent of those of the largest scales, dimensional analysis could be used to determine the relative length and time scales of turbulence. According to this theory the smallest relevant length scale present in a turbulent flow, the so called Kolmogorov length scale, is:

$$\eta \sim \left(\frac{\nu^3}{\epsilon}\right)^{1/4} \tag{3.3}$$

Where ν is the flow's kinematic viscosity, and ϵ is the rate of kinetic energy transferred from the large scales to the small scales, also known as the turbulent dissipation rate. Similarly expressions for the Kolmogorov time and velocity scales can also be found as:

$$\tau \sim \left(\frac{\nu}{\epsilon}\right)^{1/2} \tag{3.4}$$

$$v \sim (\nu\epsilon)^{1/4} \tag{3.5}$$

Using the above expressions we can determine the computational cost of DNS. If we say that our model problem has geometric length scale l_l, then in order to resolve all the relevant length scales in the flow our domain must contain at least l_l/η grid points in each direction. Since turbulent flows are inherently three dimensional the total number of grid points needed is:

$$N = N_x N_y N_z = (l_l/\eta)^3 \tag{3.6}$$

Furthermore in order to compute the unsteady dynamics of the fastest turbulent fluctuations a time step should be chosen as $\Delta t \sim \eta/u_l$ and the simulation run for many large-eddy turn over times, each with length proportional to l_l/u_l. This results in the number of times steps to be taken as:

$$N_t \sim l_l/\eta \tag{3.7}$$

From Equation 3.3 the cost can then be written as:

$$cost = N_x N_y N_z N_t \sim (l_l/\eta)^4 \sim \frac{\epsilon}{\nu^3} l_l^4 \tag{3.8}$$

An estimate for ϵ can also be found using dimensional analysis. We can say that the large eddies have kinetic energy proportional to the square of the characteristic flow velocity u_l. If we also assume that the rate of energy transfer to the smallest eddies is proportional to the large eddy turn over time, $t_l = l_l/u_l$, then we find that the rate of energy transfer is:

$$\epsilon \sim \frac{u_l^3}{l_l} \tag{3.9}$$

We can use this to determine the cost as a function of the flow's characteristic Reynolds number:

$$cost \sim \frac{u_l^3 l_l^3}{\nu^3} = \mathrm{Re}_l^3 \tag{3.10}$$

One of the largest DNS simulations ever run was that of turbulent channel flow at Re $\approx 40,000$ [26]. This Reynolds number is based on the channel core velocity and the channel height. This simulation was completed in 4 months on 2048 processors. It is clear from this example that to compute flows at the Reynolds numbers present in LEI kite problems (i.e. Re $= 3.75 - 8.44 \times 10^6$) a DNS approach won't be feasible for many years to come.

3.1.4 Turbulence Modelling

Since a DNS approach is not feasible for LEI kite flows a different approach to solving the NS equations is needed. One important realization is that for typical engineering problems one is usually only interested in the mean flow properties, and has little interest in small scale flow fluctuations. By decomposing the velocities and pressures in the NS equations into a mean and a fluctuating component, one can rewrite the NS equations as the Reynolds-Average-Navier-Stokes (RANS) equations. These can be solved on a much coarser grid, significantly decreasing the computational cost. Furthermore, if the flows investigated can be considered steady-state, that is the mean flow properties do not change significantly with time, then the time derivatives of the NS equations can be assumed to be zero, further reducing the computational time. Equation 3.11 and Equation 3.12 show the steady-state RANS equations in Einstein summation convention.

$$\overline{u_j}\frac{\partial \overline{u_i}}{\partial x_j} = -\frac{1}{\rho}\frac{\partial \overline{p}}{\partial x_i} + \frac{1}{\rho}\frac{\partial}{\partial x_j}\left(\mu\frac{\partial \overline{u_i}}{\partial x_j} - \rho\overline{u_i'u_j'}\right) \tag{3.11}$$

$$\frac{\partial \overline{u_i}}{\partial x_i} = 0 \tag{3.12}$$

Here $\overline{u_i}$ and $\overline{p}$ denote the mean components of velocity and pressure respectively. u_i' and p' denote the fluctuating components such that $u_i(t) = \overline{u_i} + u_i'(t)$ and $p(t) = \overline{p} + p'(t)$. The last terms in the brackets on the right hand side (RHS) are known as the Reynolds Stresses. The effect of turbulent fluctuations is to increase the diffusion of momentum, in much the same way that an increase in viscosity would. This is why the Reynolds Stresses are commonly placed on the RHS with the viscous diffusion term [27]. Accurately modelling the Reynolds Stresses is challenging work, and as of yet no model has been developed which provides accurate results across many different flow situations. A thorough discussion of the turbulence models available is beyond the scope of this work. However results were found in the literature which can give some guidance as to the applicability of turbulent models to the LEI kite aeroelastic problem.

Notable turbulence models include the mixing length model developed by Prandtl, the $k-\epsilon$ model developed by Launder [33], the Spalart-Almaras model [49], and the Menter Shear Stress Transport (SST) model [42]. The Menter SST model, also known as the $k-\omega\ SST$ model, has shown good results for flows with adverse pressure gradients and so is a good choice for airfoil flows [28] [42] [53]. For this reason it will be used in the rest of this work to model the Reynolds Stresses present in the LEI kite flows investigated.

$k-\omega\ SST$ Model

The specifics of Menter's $k-\omega\ SST$ turbulence model [42] are beyond the scope of this work. However, a basic understanding of how the model works is necessary in order to properly perform RANS simulations. The model contains a shear stress transport *SST* formulation, which blends the $k-\omega$ model that is used in the boundary layer with the $k-\epsilon$ model that is used in the free stream. This utilizes the strengths of both models.

The model begins, like many others, with the Boussinesq eddy viscosity assumption. This assumption links the turbulent Reynolds stresses to the mean flow gradients through a term known as the turbulent (eddy) viscosity μ_t, as shown in Equation 3.13, where δ_{ij} is the Kronecker delta.

$$-\rho\overline{u_i'u_j'} = \tau_{ij} = 2\mu_t\left(S_{ij} - \frac{1}{3}\frac{\partial \overline{u_k}}{\partial x_k}\delta_{ij}\right) - \frac{2}{3}\rho k\delta_{ij} \tag{3.13}$$

$$S_{ij} = \frac{1}{2}\left(\frac{\partial \overline{u_i}}{\partial x_j} + \frac{\partial \overline{u_j}}{\partial x_i}\right) \tag{3.14}$$

In this way the Reynolds stresses can be found from knowledge of only one parameter, the turbulent viscosity μ_t. This turbulent viscosity is in turn found from the turbulent kinetic energy k, specific turbulent dissipation rate ω, and the vorticity magnitude Ω, as shown in Equation 3.15.

$$\mu_t = \frac{\rho a_1 k}{\max(a_1\omega, \Omega F_2)} \tag{3.15}$$

$$\Omega = \sqrt{2W_{ij}W_{ij}} \tag{3.16}$$

$$W_{ij} = \frac{1}{2}\left(\frac{\partial \overline{u_i}}{\partial x_j} - \frac{\partial \overline{u_j}}{\partial x_i}\right) \tag{3.17}$$

The values of k and ω are then assumed to convect and diffuse through the flow domain in the same way that any other flow property would. As such they are governed by similar partial differential equations, as shown in Equation 3.18 and Equation 3.19 in incompressible form, which are solved using the finite volume method given the appropriate boundary conditions.

$$\frac{\partial k}{\partial t} + \overline{u_j}\frac{\partial k}{\partial x_j} = \frac{P}{\rho} - \beta^* \omega k + \frac{1}{\rho}\frac{\partial}{\partial x_j}\left((\mu + \sigma_k \mu_t)\frac{\partial k}{\partial x_j}\right) \tag{3.18}$$

$$\frac{\partial \omega}{\partial t} + \overline{u_j}\frac{\partial \omega}{\partial x_j} = \frac{\gamma}{\mu_t}P - \beta\omega^2 + \frac{1}{\rho}\frac{\partial}{\partial x_j}\left((\mu + \sigma_\omega \mu_t)\frac{\partial \omega}{\partial x_j}\right) + 2(1 - F_1)\frac{\sigma_{\omega 2}}{\omega}\frac{\partial k}{\partial x_j}\frac{\partial \omega}{\partial x_j} \tag{3.19}$$

$$P = \tau_{ij}\frac{\partial u_i}{\partial x_j} \tag{3.20}$$

$$F_1 = \tanh(arg_1^4) \tag{3.21}$$

$$arg_1 = \min\left(\max\left(\frac{\sqrt{k}}{\beta^*\omega d}, \frac{500\nu}{d^2\omega}\right), \frac{4\rho\sigma_{\omega 2}k}{CD_{k\omega}d^2}\right) \tag{3.22}$$

$$CD_{k\omega} = \max\left(2\rho\sigma_{\omega 2}\frac{1}{\omega}\frac{\partial k}{\partial x_j}\frac{\partial \omega}{\partial x_j}, 10^{-20}\right) \tag{3.23}$$

$$F_2 = \tanh(arg_2^2) \tag{3.24}$$

$$arg_2 = \max\left(2\frac{\sqrt{k}}{\beta^*\omega d}, \frac{500\nu}{d^2\omega}\right) \tag{3.25}$$

Where ρ is the flow density, ν is the flow kinematic viscosity, and d is the distance from a point to the nearest wall. The constants $\beta, \sigma_k, \sigma_\omega$, and γ have been empirically determined to tune the model such that it produces satisfactory results. The SST formulation blends these constants according to the value of F_1, as shown in Equation 3.26 where ϕ represents any of these constants.

$$\phi = F_1\phi_1 + (1 - F_1)\phi_2 \tag{3.26}$$

The empirically tuned values are shown below.

$$\gamma_1 = \frac{\beta_1}{\beta^*} - \frac{\sigma_{\omega 1}\kappa^2}{\sqrt{\beta^*}} \qquad \gamma_1 = \frac{\beta_2}{\beta^*} - \frac{\sigma_{\omega 2}\kappa^2}{\sqrt{\beta^*}} \tag{3.27}$$

$$\sigma_{k1} = 0.85 \qquad \sigma_{\omega 1} = 0.5 \qquad \beta_1 = 0.075 \tag{3.28}$$

$$\sigma_{k2} = 1.0 \qquad \sigma_{\omega 2} = 0.856 \qquad \beta_2 = 0.0828 \tag{3.29}$$

$$\beta^* = 0.09 \qquad \kappa = 0.41 \qquad a_1 = 0.31 \tag{3.30}$$

3.1.5 Flow Transition

The transition of flows from laminar to turbulent is a complex and well studied field. A complete discussion of the topic is way beyond the scope of this work. The goal of this section is only to determine how this transition can be modelled for the flows involving LEI kites, and how sensitive the results of CFD calculations are likely to be to the choice of transition model.

The effect of transition to turbulence is to delay flow separation and increase the skin friction drag [29]. It is postulated that at the large Reynolds numbers present in LEI kite flows transition will happen close to the leading edge. Following this reasoning it is assumed that the choice of transition model will have little effect on the position of trailing edge flow separation. The importance of transition is then only pertinent to the calculation of skin friction drag, with later transition resulting in a larger amount of laminar flow and a lower integral drag coefficient.

For flows on curved surfaces with pressure gradients, like those encountered with airfoils, the transition to turbulence is more complicated. For these flows other methods of predicting laminar to turbulent transition have been developed. The most common is the so called e^n method initially proposed by Smith [46] and van Ingen [51], and available for use in the 2D panel code XFOIL. Figure 3.1 and Figure 3.2 show the effect of assuming fully turbulent flow or using the e^n method when utilizing a RANS solver for airfoil performance prediction.

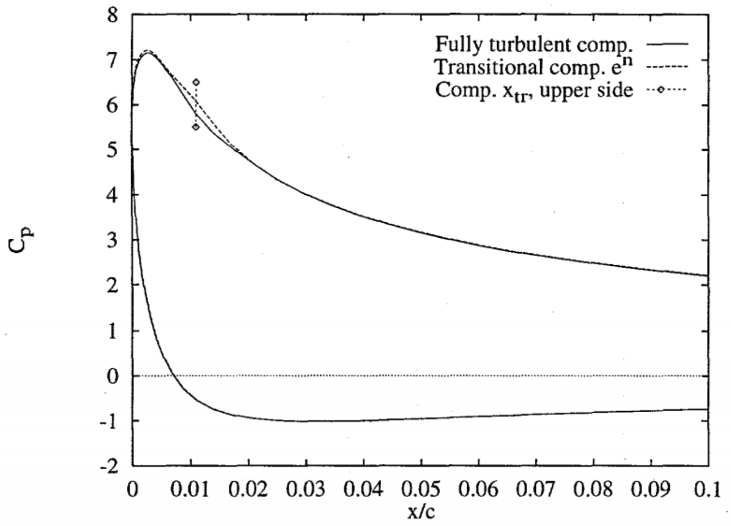

Figure 3.1: Pressure distribution, C_p, for fully turbulent flow compared with transition flow and computed transition location. NACA0012, $\alpha = 12°, \mathrm{Re} = 3 \times 10^6$. Reproduced from [28].

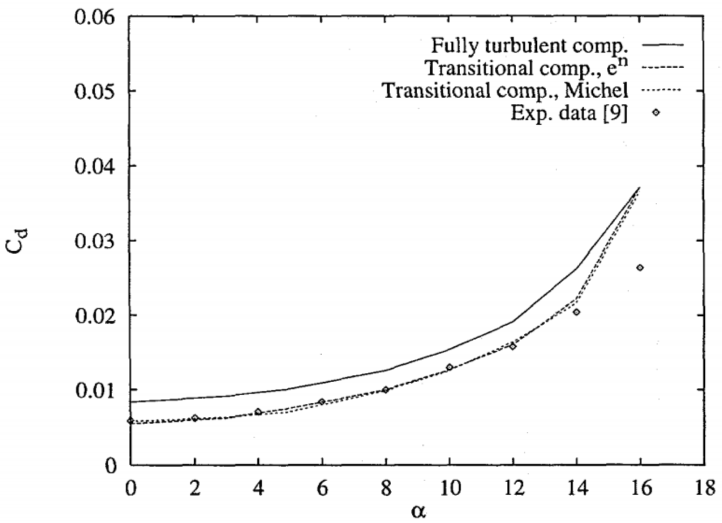

Figure 3.2: Drag curve for fully turbulent compared with transitional flow and experimental data, NACA0012, $\mathrm{Re} = 3 \times 10^6$. Reproduced from [28].

It is seen that the pressure, and therefore the lift calculations are relatively unaffected for the NACA0012 at this Reynolds number. The drag however is affected significantly by the choice of transitional model. It is also known that surface roughness, and free stream disturbances can increase the boundary layer instability and trigger transition sooner. Seams on an LEI kite, membrane flutter, dirt, and other contamination all act to increase surface roughness. These facts, along with the larger Reynolds numbers encountered in LEI kite flight point to the conclusion that transition to turbulence is likely to occur very close to the leading edge of the kite. For this reason is seems reasonable to use fully turbulent parameters in the simulation of LEI kite flows, that is the boundary layer is assumed to be turbulent throughout its length. However, without experimental verification, it is difficult to say if this approach yields correct results. As shown in Figure 3.2 one should be especially wary of any drag values predicted from a fully turbulent computation.

3.2 OpenFOAM

OpenFOAM is an open source collection of utilities and applications that can be used to solve many different vector field problems, including incompressible fluid flows. The source code is freely available under the General Public License, meaning anyone can view and alter the code as they wish. This has made it a popular choice among academic and commercial organizations alike.

OpenFOAM contains many different applications for solving many different kinds of flow problems. The simpleFoam application solves the discretized steady-state RANS equations using the finite-volume method according to the mesh, boundary conditions, turbulence models, and flow parameters specified.

3.2.1 Semi-Implicit Method for Pressure Linked Equations (SIMPLE)

Solving the steady-state RANS equations numerically is not straight forward because an explicit expression for the pressure is not available. To over come this difficulty the simpleFoam application in OpenFOAM uses the Semi-Implicit Method for Pressure Linked Equations (SIMPLE) algorithm to solve the RANS equations numerically [44]. A complete discussion of this method can be found in [53]. The general idea is to first guess a value for the pressure, and use the deficit from the continuity equations (conservation of mass) to obtain a pressure correction. This is repeated until the solution converges.

The algorithm can be summed up as follows.

1. Set the boundary conditions.
2. Solve the discretized momentum equations to compute the intermediate velocity field.
3. Compute the mass fluxes at the cell faces.
4. Solve the pressure equation and apply under-relaxation.

5. Correct the mass fluxes at the cell faces.
6. Correct the velocities on the basis of the new pressure field.
7. Update the boundary conditions.
8. Repeat till convergence.

Steps 4 and 5 can be repeated a prescribed number of times to correct for the effects of mesh non-orthogonality. In OpenFOAM this is specified in the `fvSolution` file with the key word `nNonOrthogonalCorrectors`. A complete desciption of this correction process can be found in [39]. Mesh non-orthogonality is discussed further in subsection 3.3.3.

3.3 Meshing

In order to mesh the kite the commercial software Pointwise was used. In order to become familiar with the software, and to validate the solution parameters used with the software OpenFOAM, a number of 2D meshes were also created. This section discusses the meshing process and the various decisions that were made.

3.3.1 2D Meshing

For the 2D meshes the hyperbolic mesh extrusion algorithm was used to create a high quality structured O-Mesh of the airfoils being investigated. An example of this type of mesh can be seen in Figure 3.3.

The number of points around the airfoil, and the total radius of the O-Mesh were varied in order to determine their effect on solution accuracy, as discussed in section 4.1. The height of the first boundary layer cell was selected according to the method discussed in subsection 3.3.4.

3.3.2 3D Meshing of V2

Using a similar approach to the 2D meshing, a 3D structured kite mesh was created cross-section by cross-section. Since no consideration of yawed inflow has been considered in this work, and since the flow solver (simpleFOAM) assumes a steady-state flow solution, there is no reason to mesh the entire kite. Any solution found will be symmetric about the mid span of the kite. Therefore, in order to save computational cost, only half of the kite was meshed, and a symmetry plane boundary condition was imposed at the mid span location.

The geometry of the kite was taken from Surfplan. A new output format was developed for this purpose. This format specifies a number of cross-sections, their chord, orientation, and profile shape. For the case of the V2 8 cross-sections were specified to mesh the half kite. This information was then passed to Pointwise in order to build up a structured surface mesh of the kite. It can be seen in Figure 3.4.

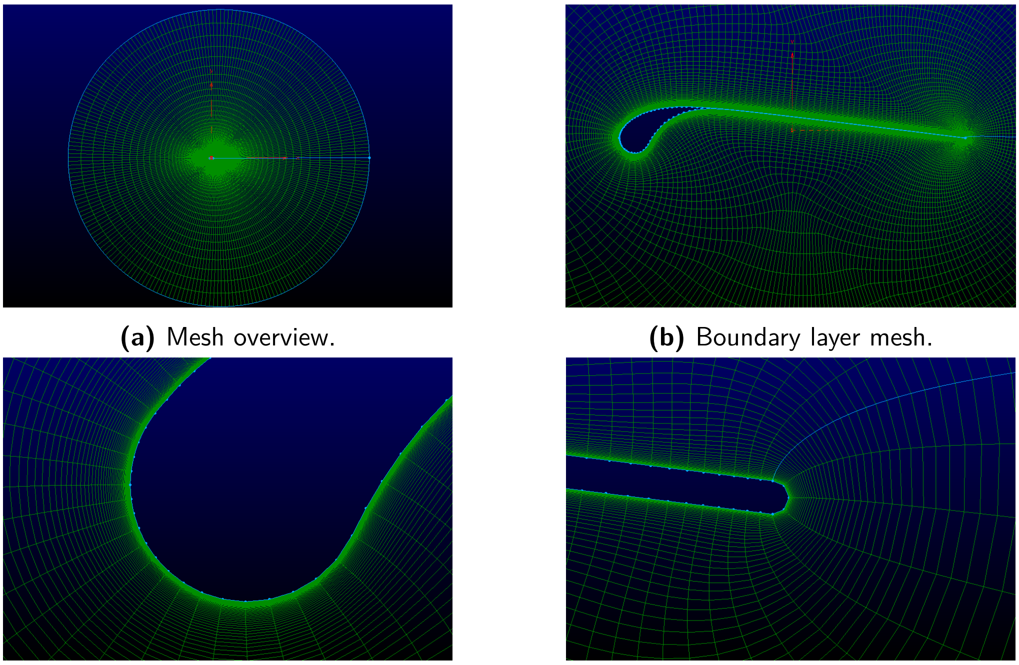

(a) Mesh overview.

(b) Boundary layer mesh.

(c) Leading edge.

(d) Trailing edge.

Figure 3.3: 2D structured hyperbolic mesh of V2 mid span cross section airfoil created in Pointwise (243x146x50).

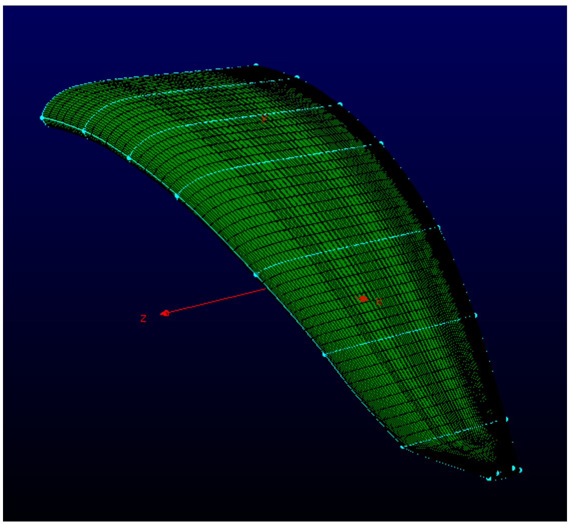

Figure 3.4: Structured surface mesh half of the V2 kite.

A number of geometric simplifications were made to the kite geometry. These simplifications greatly reduce the complexity of the meshing process. The chordwise struts have been removed and the volume behind the leading edge tube has been ‘filled in’. It is unsure what the effect of removing the struts is on the flow solution found. A discussion of the effect of ‘filling in’ behind the leading edge tube can be seen in section 4.2.

One challenge with the cross-section approach to building a 3D mesh is how to treat the tip. This problem was solved by building a special tip treatment that wraps around the tip to ensure the surface mesh is water tight. This can be seen in Figure 3.5.

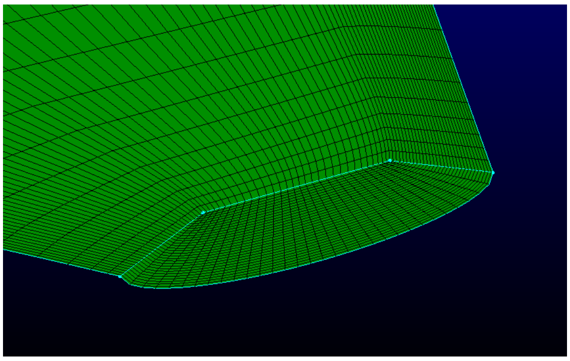

Figure 3.5: Tip treatment of the kite surface mesh.

Using this surface mesh a structured boundary layer mesh can be extruded using the hyperbolic mesh extrusion algorithm in Pointwise, similar to how it was done in 2D. The purpose of this section of the mesh is to ensure that the boundary layer is well resolved with enough cells to capture the steep velocity gradients near the wall. In this case between 70 and 80 layers were extruded. The hyperbolic mesh extrusion in Pointwise ensures that the cells are minimally skewed and well aligned with the dominant flow streamlines, thus ensuring high mesh quality. The height of the first boundary layer cell was selected according to the method discussed in subsection 3.3.4. The boundary layer mesh can be seen in Figure 3.6.

Ideally this hyperbolic mesh extrusion would be continued until the farfield to create a high quality, fully structured, hemispherical mesh. This is indeed possible for straight wings and wind turbine blades. However, in the case of the V2 kite, the hyperbolic mesh extrusion algorithm is unable to deal with the large anhedral of the kite as the cells become too squeezed. The algorithm thus becomes unstable after approximately 80 layers.

During many conversations with the Pointwise support team it was concluded that a hybrid mesh approach would be needed in which the boundary layer mesh shown in Figure 3.6 is joined with an unstructured mesh covering the rest of the domain. The completed mesh can be seen in Figure 3.7 and Figure 3.8. Several layers of unstructured mesh cells were created to control the grading of the cells in the direction normal to the kite surface. Unfortunately this approach results in many non-orthogonal cells at the boundary between the structured and structured portions of the mesh. This requires that non-orthogonal correctors be used in the flow solver in order to ensure solution stability, severely increasing the computational cost.

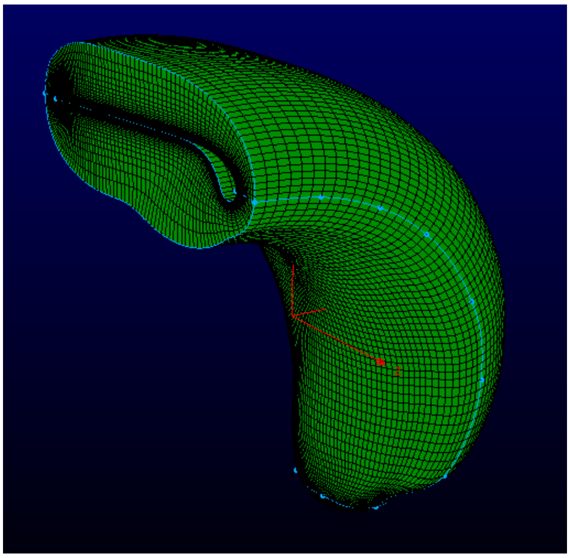

Figure 3.6: Half kite boundary layer mesh.

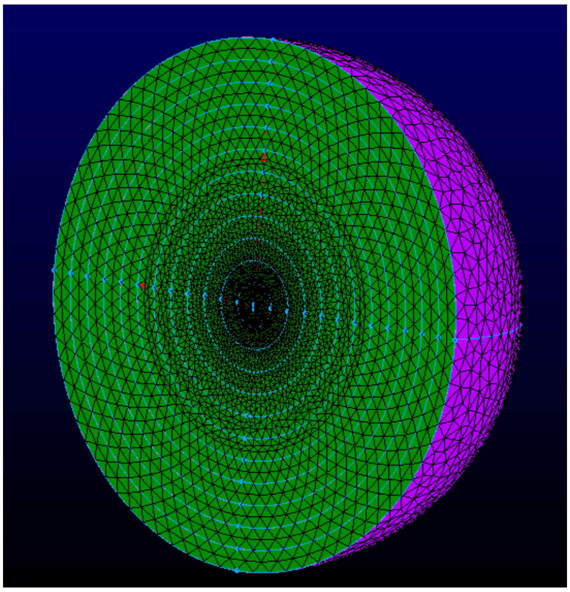

Figure 3.7: Total V2 hemispherical mesh (186x63x80x60).

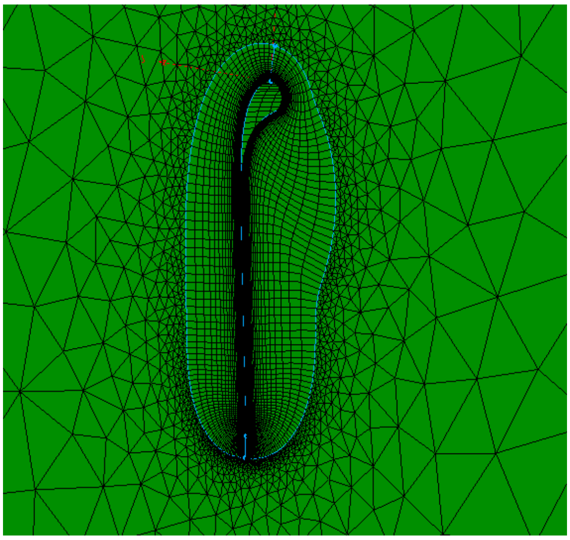

Figure 3.8: The transition of the structured BL mesh to the unstructured farfield mesh (186x63x80xr60).

3.3.3 Mesh Non-Orthogonality

Mesh non-orthogonality can cause stability issues and numerical errors. It occurs when the line joining two adjacent cell centers does not pass through the cell face at a right angle. Figure 3.9 shows two different meshes, one that is orthogonal (A) and one that is not (B).

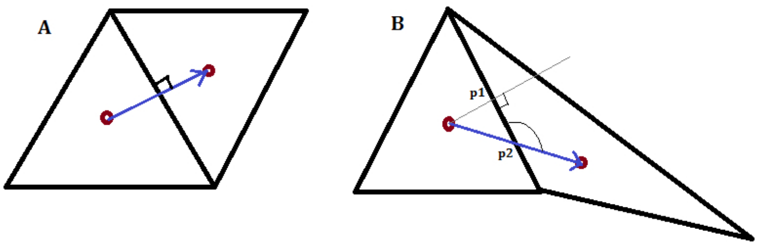

Figure 3.9: An illustration of mesh nonOrthogonality.

When building a hybrid mesh in Pointwise significant mesh non-orthogonality is found to occur on the junction between the structured boundary layer mesh and the unstructured farfield mesh. A related mesh quality metric, known as cell skewness, can be visualized in Pointwise and is shown in Figure 3.10.

On this junction the cells are unique to the entire domain in that they have one quadrilateral face and four triangular faces. In the rest of the domain the cells have either 6 quadrilateral faces (structured) or four triangular faces (unstructured). The mesh quality is the worst along a strip that runs span wise along the trailing edge portion of the boundary layer mesh. The quadrilateral faces of the cells in this region have a large aspect ratio, that is they are long and thin. This is seen in Figure 3.11. This causes cells that are long, but not very high, resulting in large cell skewness and non-orthogonality as shown

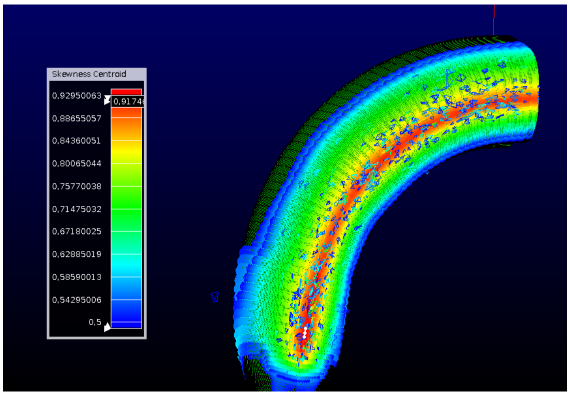

Figure 3.10: Mesh skewness, an indicator of non-orthogonality, on the junction between the boundary layer and farfield meshes.

in Figure 3.12. Unfortunately due to the need to cluster cells near the trailing edge of the airfoil it seems that this thinning of cells in this region is unavoidable. Perhaps a more creative analysis of the problem could yield a solution that the author is unaware of.

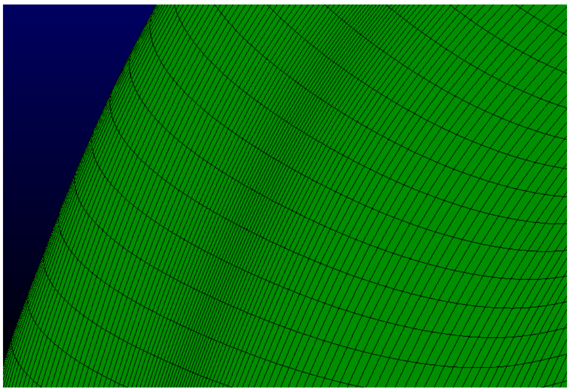

Figure 3.11: High aspect ratio of quadrilateral faces along the trailing edge of the boundary layer mesh.

3.3.4 First Boundary Layer Cell Height

In order to properly resolve the boundary layer it is important that the height of the first cell in the boundary layer, measured in non-dimensional wall units, is on the order of 1, as shown in Equation 3.31. This holds true for both the 2D and the 3D meshes that were created. This ensures there are enough cells to resolve the linear viscous sublayer. However, prior to running the simulation the value of u^* is unknown, hence it is not known how large to make the first layer of cells in the boundary layer. Luckily an estimate of the cell height can be made from flat plate boundary layer relations [56]. The approximate first cell height used is calculated from Equation 3.34 with $x = c$, and will be checked later.

$$y^+_{\Delta s} = \frac{u^* \Delta s}{\nu} = \mathcal{O}(1) \tag{3.31}$$

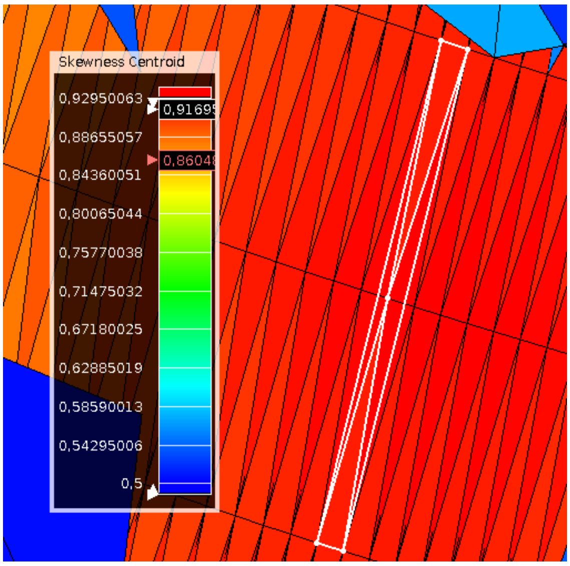

Figure 3.12: Highly skewed and non-orthogonal cell caused by large aspect ratio quadrilateral face.

$$u^* = \sqrt{\frac{\tau_w}{\rho}} \tag{3.32}$$

$$C_f = \frac{\tau_w}{\frac{1}{2}\rho U_\infty^2} = \frac{0.027}{\mathrm{Re}_x^{1/7}} \tag{3.33}$$

$$\Delta s = 8.61 x^{1/14} \left(\frac{\nu}{U_\infty}\right)^{13/14} \tag{3.34}$$

3.3.5 Mesh Naming

In order to investigate the effect of mesh grading on the solution several different meshes were created. In order to make it easier to discuss which mesh was used a mesh naming convention was adopted.

For 2D meshes three numbers are given which describe the number of mesh points surrounding the airfoil, the number of mesh points normal to the airfoil, and the distance from the airfoil to the farfield in chords (i.e. 186x80x60). In 3D four numbers are given that describe the number of points surrounding the airfoil, the number of points in the spanwise direction excluding the tip treatment, the number of points around the circumference of the farfield mesh, and the distance from the kite to the farfield boundary in mid-span chords (i.e. 186x63x80x60).

3.4 Simulation Settings

3.4.1 Turbulence Models

The two equation *k*-*ω* *SST* model, a well established model used widely in the aerospace field, was chosen to close the RANS equations. This model is discussed in section 3.1.4.

3.4.2 Boundary Conditions

The simulation boundary conditions were chosen to give the flow the desired Reynolds number and also to approximate the turbulence levels found in the real LEI kite flight. In all the simulations a Reynolds number of 6 million was used.

Shown in Table 3.1 and Table 3.2 are the boundary conditions used in the farfield and airfoil surface respectively.

Table 3.1: Farfield Boundary Conditions

Flow Variable	Type	Value
Velocity Magnitude	inletOutlet	$\frac{\mathrm{Re}\cdot\nu}{c}$
Relative Pressure	outletInlet	$0\,\mathrm{Pa}$
k Turbulent Kinetic Energy	inletOutlet	$0.0031\,\mathrm{m^2/s^2}$
ω Specific Turbulent Dissipation Rate	inletOutlet	$23.7 \times 10^3\,\mathrm{s^{-1}}$

Table 3.2: Boundary Conditions Applied at Airfoil Surface

Flow Variable	Type	Value
Velocity Magnitude	fixedValue	$0\,\mathrm{m/s}$
Relative Pressure	zeroGradient	-
k Turbulent Kinetic Energy	fixedValue	$0\,\mathrm{m^2/s^2}$
ω Specific Turbulent Dissipation Rate	fixedValue	$1 \times 10^8\,\mathrm{s^{-1}}$

Generally for external aerodynamic applications it is advised to specify a fixed velocity and zero pressure gradient at the inlet, and a zero velocity gradient and fixed pressure at the outlet. Unfortunately for the O-Mesh and hemispherical mesh topologies it is difficult to know before hand which parts of the farfield will be inlets and which outlets, particularly if one wants to investigate flows are varying angles of attack. For this reason the `inletOutlet` and `outletInlet` boundary types are available for use in OpenFOAM. The `inletOutlet` specification applies a fixed value (i.e. Dirichlet) condition to any parts of the boundary where flow is entering the domain, and a fixed gradient of zero (i.e. Neumann) condition to any part of the boundary where flow is leaving the domain. The `outletInlet` specification does the reverse, applying a fixed value to outflow and a zero fixed gradient to inflow.

3.4.3 Finite Volume Schemes

A complete description of the finite-volume method is not needed in this work as many great references already exist (see [53] for example). However the point of discretization schemes will be discussed here shortly in relation to LEI kite aerodynamics. One of the principal problems involved with using the finite-volume method to solve convection-diffusion problems (like the RANS equations) is the calculation of the value of the transported value ϕ (could be mass, momentum, turbulent kinetic energy, etc.) at the cell faces. Consider the 1D convection diffusion problem as illustrated below in Figure 3.13.

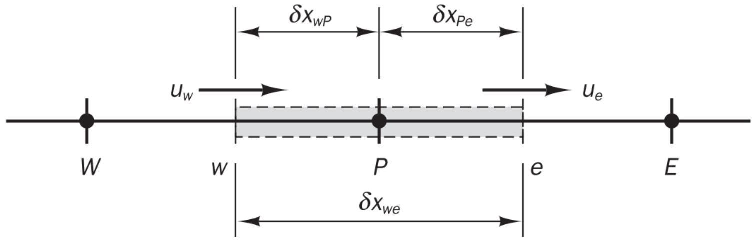

Figure 3.13: The finite-volume method applied to a 1D convection-diffusion problem. Reproduced from [53].

The finite volume method balances the convective and diffusive fluxes of ϕ across the control volume boundaries with the accumulation of ϕ within the control volume. Typically the values of ϕ are stored at the cell nodes (P) and are average cell values. This leaves the problem of how to determine the values of ϕ at the cell faces (w,e), values that are needed to compute the fluxes across the cell boundaries.

The *Central-Differencing scheme* (CD) simply takes the average of the two neighboring nodes as the value of ϕ at the cell boundary. This works well for problems that are dominated by diffusive processes. That is Pe < 2, where Pe is the cell Peclet number defined in this context according to Equation 3.35, where L is the chractersitic length of the cell, Sc_t is the turbulent Schmidt number, ν_t is the turbulent eddy viscosity, and K is the turbulent eddy diffusivity.

$$\mathrm{Pe} = \frac{LU}{D} = \mathrm{Re}_L \cdot \mathrm{Sc}_t = \frac{U L}{\nu} \frac{\nu_t}{K} \tag{3.35}$$

For low Peclet numbers the value of ϕ in one cell influences more or less evenly the values of ϕ in all neighboring cells. However, for processes dominated by convection, Pe > 2, this no longer holds. Using the CD scheme in these cases can lead to numerical instabilities (so called *wiggles*). The solution is the adoption of other schemes that lend more importance to the value of ϕ in the nodes upwind of the cell face (so called *Upwind* schemes). Figure 3.14 shows why for high Peclet numbers this approach produces a more suitable estimate of ϕ at the cell face.

The simplest *Upwind* scheme is the *Upwind Differencing* scheme UDS. This scheme simply takes the value of the node directly upwind of the cell face as the value of ϕ at the cell face. This scheme works well but can lead to a numerical phenomenon known as false diffusion in coarse meshes where the flow is not aligned with the main cell direction.

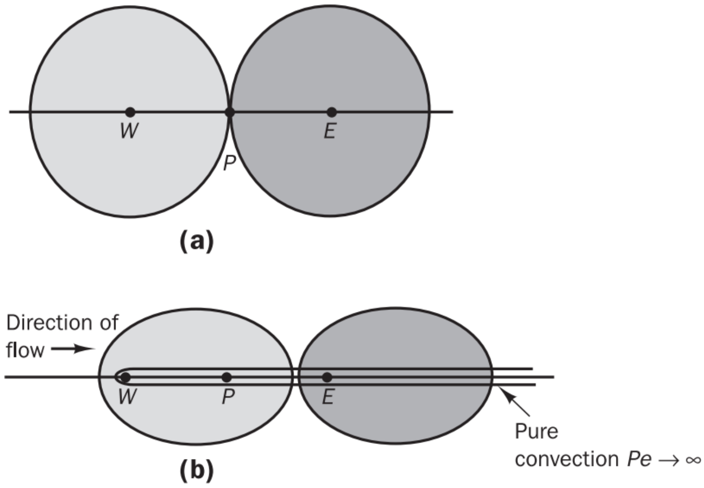

Figure 3.14: The influence of Pe on the distribution of ϕ in convection-diffusion problems. Reproduced from [53].

For the simulations being done on LEI kites the Reynolds numbers are high, and the need for a reduced number of cells is paramount to keep computational costs reasonable. For these reasons the cell Peclet numbers encountered will be high and necessitate the need for using an upwind scheme.

Shown in Table 3.3 are the finite volume schemes used to discretize the governing equations. The `upwind` and `linearUpwind` schemes were chosen for the divergence terms because of the large flow velocities in the domain.

Table 3.3: Finite Volume Schemes

Gradient	Gauss linear
Laplacian	Gauss linear limited 0.5
Divergence (U)	bounded Gauss linearUpwind
Divergence (k, ω, $\tilde{\nu}$)	bounded Gauss upwind

3.4.4 Solution Parameters

OpenFOAM allows the user to control a number of options that determine how the matrices created by the SIMPLE algorithm are solved, to what tolerances, and using what relaxation factors. The precise function of each of these settings can be found in the OpenFOAM documentation. The settings used for all the simulations are shown in Table 3.4. The setting `nNonOrthogonalCorrectors` is particularly important for hybrid meshes, such as those used in the 3D simulations, where cells at the boundary between the structured boundary layer mesh and unstructured farfield mesh can become significantly non-orthogonal. More about this setting can be seen in subsection 3.2.1.

Table 3.4: Solution Parameters

Matrix Solver (p)	PCG
Matrix Solver (U,k,ω)	PBiCG
tolerance (p,U,k,ω)	1×10^{-8}
relTol (p,U,k,ω)	0.01
Relaxation Factor (P)	0.3
Relaxation Factor (U,k,ω)	0.7
nNonOrthogonalCorrectors (2D)	0
nNonOrthogonalCorrectors (3D)	4 depending on mesh

Chapter 4

Results

4.1 NACA0012

The solution settings described in section 3.4 were validated by simulating the 2D, steady state flow around the well studied NACA0012 airfoil. The results were compared against data from [25], [32], and [1]. Table 4.1 and Table 4.2 describe the comparison data that was used. Also used was McCroskey's best fit $\partial C_l/\partial\alpha$ curve found from [40] shown in Equation 4.1. Three meshes were investigated, built as described in section 3.3 with sizes of 150x100xr150, 250x150xr150, and 600x150xr150. Simulations were run at a Reynolds number of 6×10^6.

Table 4.1: Summary of comparison data.

Data Set	Re	Ma	Boundary Layer Treatment
Gregory	2.88×10^6	Approx. Incompressible	Smooth surface
Ladson (1988)	6×10^6	0.15	Transition strips at 5% chord
NASA CFL3D	6×10^6	Incompressible	Fully Turbulent CFD

Table 4.2: Measurements available from data sets.

Data Set	C_l, C_d	C_p	C_f
Gregory	✓	✓	✗
Ladson (1988)	✓	✓	✗
NASA CFL3D	✗	✗	✓

$$\partial C_l/\partial\alpha = (0.1025 + 0.00485 \log_{10}(\mathrm{Re}/10^6))/(1 - \mathrm{Ma}^2) \tag{4.1}$$

4.1.1 Lift and Drag

Summaries of the relative error are shown in Table 4.3 and Table 4.4 with a positive value indicating that the OpenFOAM solution was greater than the reference. The OpenFOAM results on the finest mesh under predict the lift by less than 7% against all the reference data presented. This agreement is considered to be very good, considering that there is a similar spread in the experimental data.

The drag predictions are off by as much as 73% compared with the Ladson data. This is a somewhat surprising result, and highlights the difficulty of simulating the drag of streamlined bodies.

Table 4.3: Summary of C_l relative error.

Mesh	α	vs Gregory	vs Ladson	vs CFL3D	vs McCroskey
600x150x150	10°	-1.3%	0.8%	-2.2%	1.8%
	15○	-2.0%	-1.5%	-4.9%	-6.5%
250x150x150	10°	-3.1%	-1.0%	-3.9%	0.0%
	15○	-7.8%	-7.4%	-10.5%	-12.0%
150x100x150	10°	0.5%	2.6%	-0.4%	3.6%
	15○	-4.5%	-4.0%	-7.3%	-8.8%

Table 4.4: Summary of C_d relative error.

Mesh	α	vs Gregory	vs Ladson	vs CFL3D
600x150xr150	0°	25.7%	7.3%	5.9%
	10°	16.3%	31.4%	27.2%
	15○	10.4%	72.8%	49.3%
250x150x150	0°	23.6%	5.6%	4.2%
	10°	13.5%	28.3%	24.2%
	15○	10.5%	72.9%	49.4%
150x100x150	0°	27.6%	9.0%	7.6%
	10°	23.1%	39.1%	34.7%
	15○	31.2%	105.4%	77.4%

This comparison highlights the level of accuracy and repeatability obtainable from RANS simulations and experimental trials. In general lift values across simulations and different experiments can be found to agree to within a few percentage points. Since lift is mainly a consequence of pressure, this points to the conclusion that the RANS simulations are able to model the pressure distribution across the airfoil very well. The pressure distribution found from the finest mesh for the case of $\alpha = 15°$ can be seen in Figure 4.1. It is seen that the agreement to the experimental data is very good.

Drag values however can vary by a considerable margin. This is especially true in the case of streamlined bodies in which skin friction is responsible for the majority of the drag. Unfortunately only the skin friction data from the top surface of the airfoil from

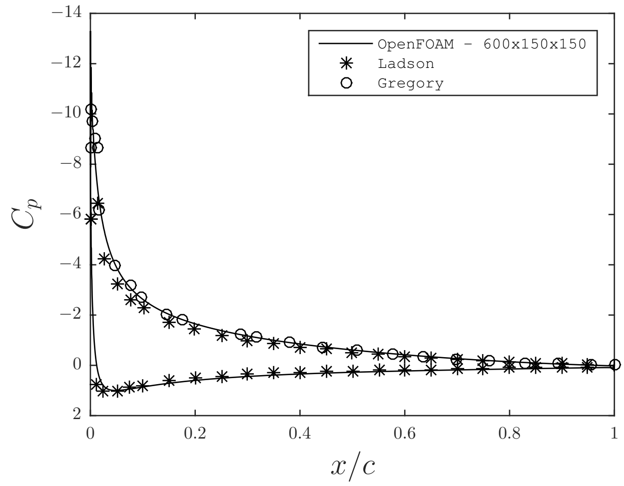

Figure 4.1: Pressure coefficient found in OpenFOAM for $\alpha = 15°$ compared with experimental results.

the CFL3D simulations is available here for comparison. It can be seen in Figure 4.2 that there is good agreement between the OpenFOAM simulations and the CFL3D simulations. The most likely reason for the large differences in drag comes down to small differences in pressure drag, which when applied to a streamlined body such as this, result in large relative differences in total drag. This would mean that in the context of LEI kites, in which large flow separations behind the leading edge tube cause significant pressure drag, the slight discrepancies in pressure would result in much smaller relative changes in total drag.

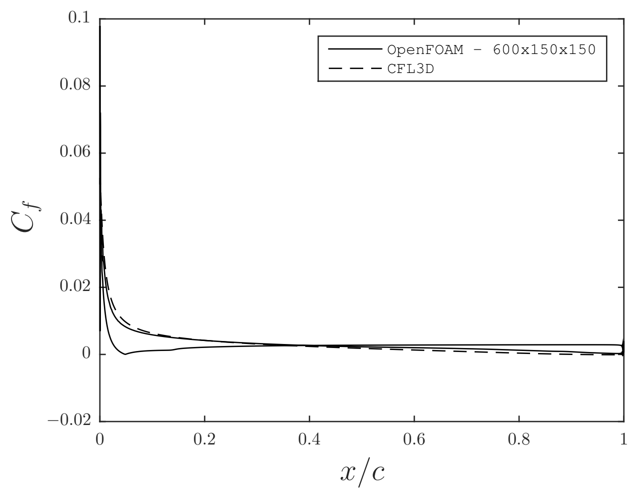

Figure 4.2: Skin friction coefficient found in OpenFOAM for $\alpha = 15°$ compared with CFL3D results.

4.1.2 First Cell Height

In order to ensure that the choice of first cell height was sufficient small to correctly resolve the boundary layer the height of the first cell was calculated in y^+ units. It was found that for all angles that the first cell height was sufficiently small. Figure 4.3 shows the first cell height for $\alpha = 15°$.

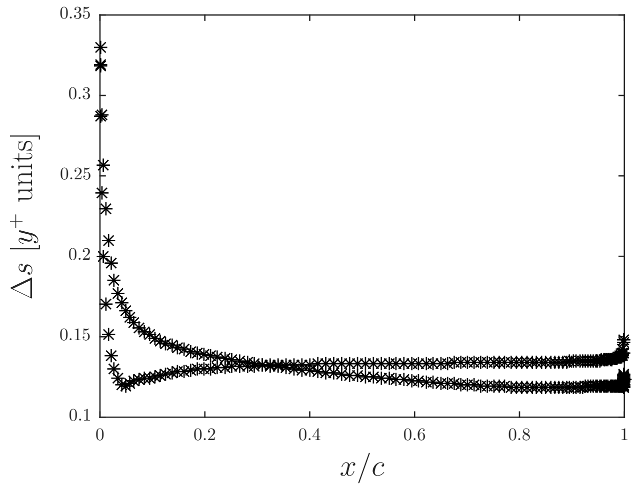

Figure 4.3: First cell height in y^+ units for $\alpha = 15°$, mesh is 250x150x150.

4.1.3 Turbulence Decay

An interesting result from the NACA0012 simulations is the realization that the turbulence imposed at the farfield boundaries may have very little effect on the solution. It can be seen from Figure 4.4 and Figure 4.5 that the farfield turbulent parameters chosen decay rather quickly. This is an interesting result and points to the conclusion that the farfield turbulence parameters make little difference to the solution. This is investigated further with the 3D simulations of the V2 kite.

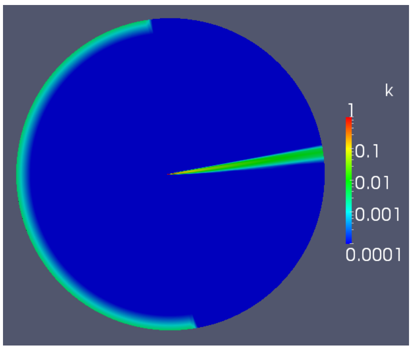

Figure 4.4: The decay of k from the farfield to the airfoil surface at $\alpha = 10°$. Note the logarithmic axis. Also the maximum shown on the scale does not correspond to the maximum found in the domain.

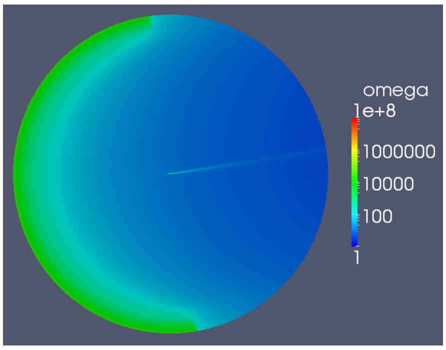

Figure 4.5: The decay of ω from the farfield to the airfoil surface at $\alpha = 10°$. Note the logarithmic axis. Also the maximum shown on the scale does not correspond to the maximum found in the domain.

4.2 Filling in the Tube

In order to investigate the effect of filling in behind the leading edge tube a two dimensional analysis was performed on the mid span cross section of the V2 kite. Two meshes were created, one that is ‘tight’ behind the leading edge tube and one that is ‘filled in’. The meshes were both the same size, 730x150x60, and can be seen in Figure 4.6.

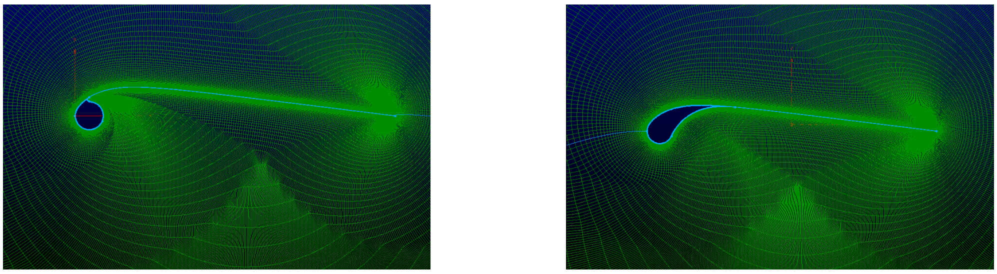

(a) Tight mesh. **(b)** Filled in mesh.

Figure 4.6: The meshes used to investigate the effect of 'filling in' behind the leading edge tube.

Lift and drag values for the two airfoils are shown in Figure 4.7. It can be seen that across a large range of angles the lift and drag values agree to within 5%, which is within the range of error found for the NACA0012 simulations, as discussed in subsection 4.1.1. At low angles of attack significant flow separation is seen to occur behind the leading edge tube. Under these conditions it would appear that filling in behind the tube has a larger effect on the solution than at slightly higher angles where less flow separation occurs behind the tube. At angles of attack larger than 18° flow separation is seen to occur from the suction surface of the airfoil. It is therefore reasoned that the discrepancies at the high angles of attack are not caused by differences in mesh (filled or tight), but rather due to difficulties replicating a flow solution due to the convergence issues at high angles of attack discussed in section 5.1.

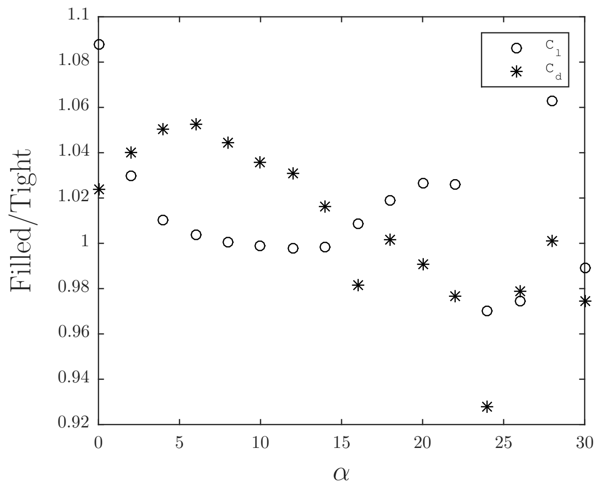

Figure 4.7: Comparison of the lift and drag values found for the filled in and tight meshes.

4.3 3D V2 LEI Kite

4.3.1 Mesh Resolution

In order to investigate the effect of mesh resolution on the solution 3 different meshes were investigated, as shown in Table 4.5. In all three meshes the farfield boundary was kept at 40 mid span chords away from the kite and the first boundary layer cell height was kept constant according to Equation 3.34. The number of cells around the airfoil, in the span wise direction, and around the circumference of the farfield boundaries were changed. All simulations were run at $\alpha = 10°$. The integral lift and drag values found were compared to the finest mesh of size 510x178x200x40. The results are shown in Table 4.6 where a positive number means the value found was larger than the reference.

Table 4.5: Description of meshes used for grid study (millions of cells).

Mesh	Boundary Layer Cells	Unstructured Cells	Total Cells
186x63x80x40	1.05	0.64	1.69
306x102x120x40	2.71	1.83	4.54
510x178x200x40	8.90	6.25	15.15

Table 4.6: Integral lift and drag error compared to 510x178x200x40 at $\alpha = 10°$.

Mesh	C_L Error	C_D Error
186x63x80x40	1.2%	-1.8%
306x102x120x40	1.2%	-1.4%

The agreement between the three meshes is very good with errors of less than 5%. The coarser meshes under predict the drag and over predict the lift.

Although the integral values of lift and drag were found to be in close agreement, it is also of interest to check the local values of pressure to determine the effect of grid resolution on the solution. Shown in Figure 4.8 are the C_p distributions found at the mid span location of the kite using the three different meshes. It can be seen that the agreement on the suction side of the kite is very good. Behind the leading edge tube on the pressure side some disagreement can be seen. This disagreement could be caused by the change in mesh resolution, or more likely it is caused by the unsteadiness of the flow in the separated region behind the leading edge tube. This is discussed in more detail in section 5.1.

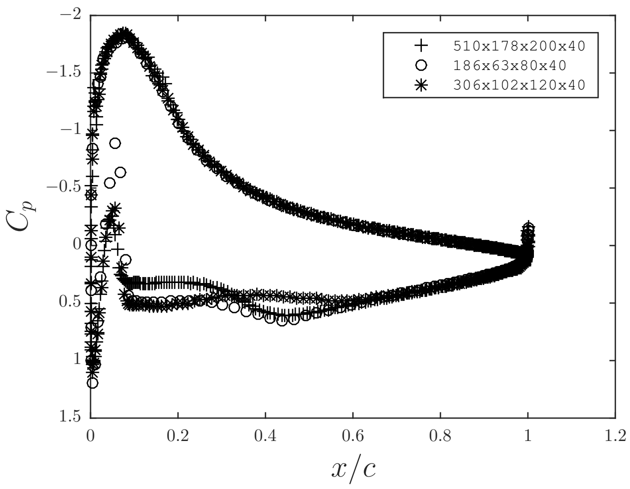

Figure 4.8: Pressure coefficient at mid-span for the different meshes, $\alpha = 10°$.

Since the agreement between the coarsest mesh is so close to that of the very finest mesh, the 186x63x80x40 mesh will be used for all future simulations in order to save on computational resources.

4.3.2 Domain Size

In order to investigate the effect of the total size of the flow domain on the solution 4 different meshes were created with domain sizes of 20,40,60, and 80 mid-span chords. Simulations were performed on the V2 kite at $\alpha = 10°$. The differences in lift and drag coefficients can be seen in Table 4.7 as compared to the 186x63x80x80 mesh. Positive errors indicate that the values found were larger than the reference.

Table 4.7: Integral lift and drag error compared to 186x63x80x80 at $\alpha = 10°$.

Mesh	C_L Error	C_D Error
186x63x80x20	-0.8%	-0.8%
186x63x80x40	-0.5%	-0.5%
186x63x80x60	-0.2%	-1.1%

It can be seen that the differences in lift and drag coefficients with changes in flow domain size are less than 1%. Based on these results a domain size of 60 mid span chords was chosen because it was noticed that solution convergence was slightly quicker with this farfield size.

4.3.3 First Cell Height

As with the case of the NACA0012, it is important that the first cell height be small enough to properly resolve the boundary layer. This parameter was not varied in the grid study discussed in subsection 4.3.1 because it was assumed that so long as the cells are thin enough to properly resolve the boundary layer no change in solution will result. As discussed in subsection 3.3.4 the approximate first cell height is given by Equation 3.34. Figure 4.9 shows the actual height in y^+ units of the first boundary layer cell at the mid span chord, and it is found to be less than 1 indicating that it is fine enough to resolve the boundary layer properly.

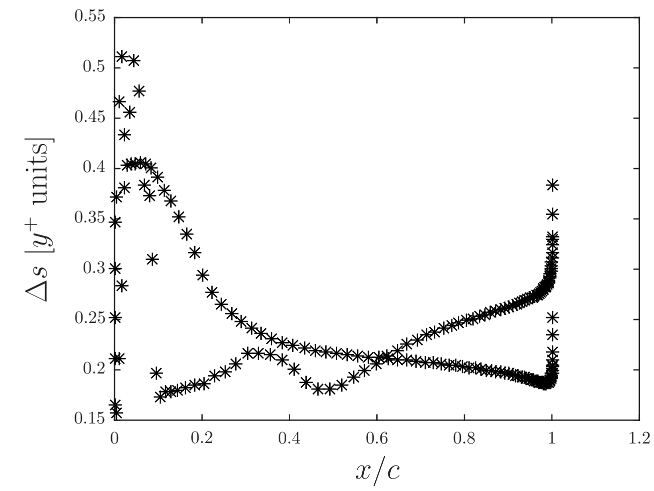

Figure 4.9: First cell height in y^+ units at the mid span for $\alpha = 10°$.

4.3.4 Turbulence Boundary Conditions

It was mentioned in subsection 4.1.3 that for the 2D simulations of the NACA0012 airfoil the turbulence introduced at the boundaries of the domain quickly decays to zero such that the values imposed at the boundaries should make little difference to the final solution. This assumption was tested for the 3D simulations performed on the V2 kite. Three different turbulent boundary conditions were specified and their results were compared as shown in Table 4.8. It can be seen that the turbulence imposed at the farfield boundaries makes less than a 1% difference in the integral lift and drag solution.

Table 4.8: Integral lift and drag results for different turbulent boundary conditions. $\alpha = 10°$, mesh is 186x63x80x60.

Turb. Intensity	k [m^2/s^2]	ω [s^{-1}]	$\frac{C_L - C_{L,norm}}{C_{L,norm}}$	$\frac{C_D - C_{D,norm}}{C_{D,norm}}$
Normal - 0.052%	3.11×10^{-3}	2.37×10^4	-	-
High - 0.5%	0.29	2.19×10^6	0.2%	-0.3%
Low - 0.005%	2.9×10^{-5}	219	-0.1%	0.0%

4.3.5 Integral Lift and Drag

Shown in Figure 4.10 are the integral lift and drag values found for the V2 kite using the mesh discussed in subsection 4.3.1. Shown for comparison are linear results obtained from Prandtl's Lifting-Line-Theory (LLT). This theory is summarized by Equation 4.2 and Equation 4.3.

$$C_L = a(\alpha - \alpha_{L=0}) \tag{4.2}$$

$$C_D = C_{D,L=0} + \frac{C_L^2}{\pi e AR} \tag{4.3}$$

Where $a = \frac{dC_l}{d\alpha}$ is the 3D lift curve slope, $\alpha_{L=0}$ is the zero-lift angle of attack, $C_{D,L=0}$ is the drag of the wing at zero lift, and e is the span efficiency factor that corrects for the non-elliptical lift distribution over the wing. Here it should be noted that Prandtl developed LLT in the context of planar wings which is clearly not the case for LEI kites. However it is hoped that comparison with LLT can yield some insights into the non-linear behavior of LEI kite flows.

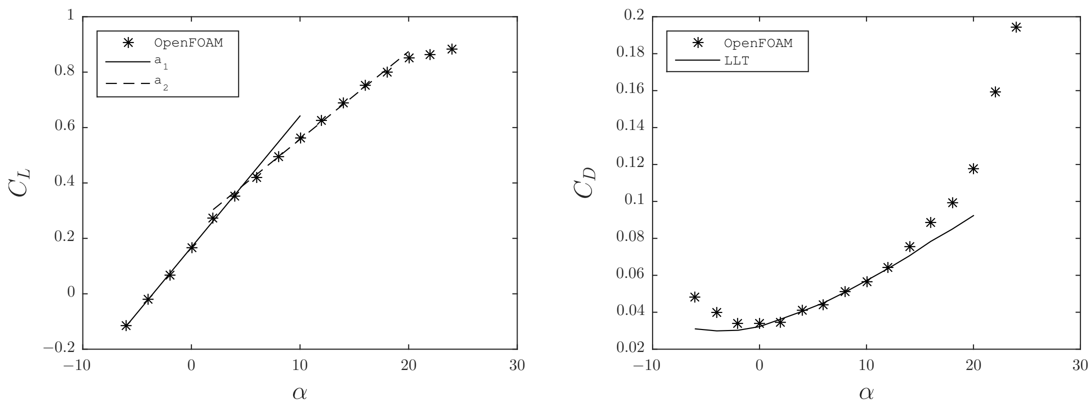

(a) Lift coefficient. **(b)** Drag coefficient.

Figure 4.10: Comparison of V2 lift and drag with linear Lifting-Line-Theory.

Shown in Table 4.9 are the constants found from a least squares fit of the integral lift and drag data with the LLT theory using an aspect ratio of $AR = 5.3$.

Table 4.9: Lifting line theory parameters.

$C_{D,L=0}$	0.0384
$\alpha_{L=0}$	$-3.54°$
$C_{D,min}$	0.0339
$\alpha_{C_{D,min}}$	$-2°$
a_1 [1/rad]	2.72
a_2 [1/rad]	1.82
e	0.70

The first manner in which the results found differ from LLT is in the clearly visible change in lift curve slope at approximately $\alpha = 4°$. This is shown in Figure 4.10a and Table 4.9 as a_1 and a_2. A least squares fit of the data for angles $-6° : 4°$ was used to find a_1. The data at the angles $6° : 18°$ was used to find a_2. At low angles of attack large flow separation exists behind the leading edge tube, artificially reducing the camber of the airfoil and decreasing the lift causing a_1 to be greater than a_2.

The second major difference is in the difference the minimum drag, and the drag at zero lift. Since $C_L^2 \geq 0$, $C_{D,L=0}$ should be the minimum drag found at any angle of attack. This is not the case for the V2 kite, where $C_{D,L=0} = 0.0384$ at $\alpha_{L=0} = -3.54°$ while the minimum drag, $C_{D,min} = 0.0339$, is found at $\alpha_{C_{D,min}} = -2°$. This difference is again thought to be caused by the flow seperations that occur behind the leading edge tube at low angles of attack. It should be noted that the LLT line drawn in Figure 4.10b and the value of e were found using $C_{D,min}$ as shown in Equation 4.4 in order to try to account for this effect.

$$C_D = C_{D,min} + \frac{C_L^2}{\pi e AR} \tag{4.4}$$

Above $\alpha \approx 18°$ the flow begins to separate off the suction surface of the kite. This leads to the large increase in drag and significant reduction in lift curve slope that is seen. This flow separation is considered in more depth in subsection 4.3.7.

4.3.6 Kite Performance

As discussed in subsection 1.2.1 the performance of a kite power system is perhaps best evaluated by the parameter $\frac{C_L^3}{C_{D,eff}^2}$. The value of $C_{D,eff}$ can be found from Equation 4.5.

$$C_{D,eff} = C_D + C_{D,p} \tag{4.5}$$

Where $C_{D,p}$ is the parasitic drag due to the tether and bridle lines. The exact quantification of $C_{D,p}$ depends entirely on the system design, and is thus hard to estimate when only considering the performance of the kite as is done here. Never the less some insight into how the kite performs can be gained by evaluating $\frac{C_L^3}{C_{D,eff}^2}$ at all angles of attack, for many different values of $C_{D,p}$. This is shown in Figure 4.11.

As can be seen, regardless of the parasitic drag the kite seems to perform best in conditions close to stall, and at angles of attack somewhere between 14° and 20°, with larger parasitic drag pushing the optimal point towards higher angles and lift coefficients. This is a somewhat surprising result as it seems to conflict with the data presented in Figure 2.3. This is discussed further in section 5.3.

4.3.7 Flow Separation

Flow separation is the most significant non-linear phenomena that occurs in LEI kite flight. Determining how and where the flow separates from the surface of the kite could

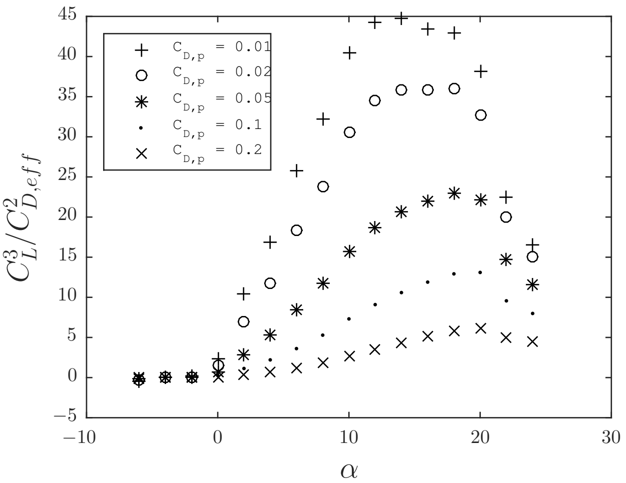

Figure 4.11: Kite performance metric applied for differing parasitic drag values.

yield important insights that could be used to adjust linear flow models to account for these effects. For this reason significant attention is given to the topic in this section.

Shown in Figure 4.12 is the development of the flow separation phenomenon off of the suction surface of the kite. Here the wall shear stress in the chordwise direction is used as an indicator of where the flow is separating. Negative values of wall shear stress indicate areas of flow recirculation and separation.

It can be seen that flow separation begins between angles of 18° and 20°. This causes a deviation from linear theory, an increase in drag and a decrease in lift, as shown in Figure 4.10. Interestingly the flow begins to separate first from the quarter span area, even though the geometric angle of attack in this area is reduced due to the kite's anhedral. The reason for this phenomena is not yet known. Some reasons could be a decreased downwash in the area due to the complex lift distribution across the kite, or the slightly different airfoil cross-section in this region. None the less this phenomena should be studied more carefully.

It would be a good time now to point out the problems of investigating flow separation using a steady state solver such as simpleFoam. Flow separation is fundamentally an unsteady phenomena, so any results obtained from a steady solver are likely to be inaccurate. It can be seen that at high angles of attack it is much more difficult to obtain solution convergence, or indeed even know if solution convergence has been reached. This is discussed in further detail in section 5.1. This difficulty can be seen in Figure 4.13, where the separation pattern changes wildly even as the flow residuals remain more or less unchanged between snap shots. Solution residuals can be found in Appendix A. The results presented in this section, therefore, should be understood as only an approximation of reality.

Behind the leading edge tube significant flow separation is seen to occur as well in LEI kite flows. This can be seen in Figure 4.14. Unlike separation from the suction side of the kite, these separation areas tend to grow in size as the angle of attack is decreased. This causes a reduction in effective camber, an increase in drag, and a reduction in lift at angles below approximately 4° as seen in Figure 4.10.

It can be seen that significant flow separation exists behind the kite even at the high angle of 22°. This points to the conclusion that any linear aerodynamic model must account for these effects even at these large angles. In a similar manner to separation from the suction surface of the kite, separation behind the leading edge tube leads to considerable solution convergence issues.

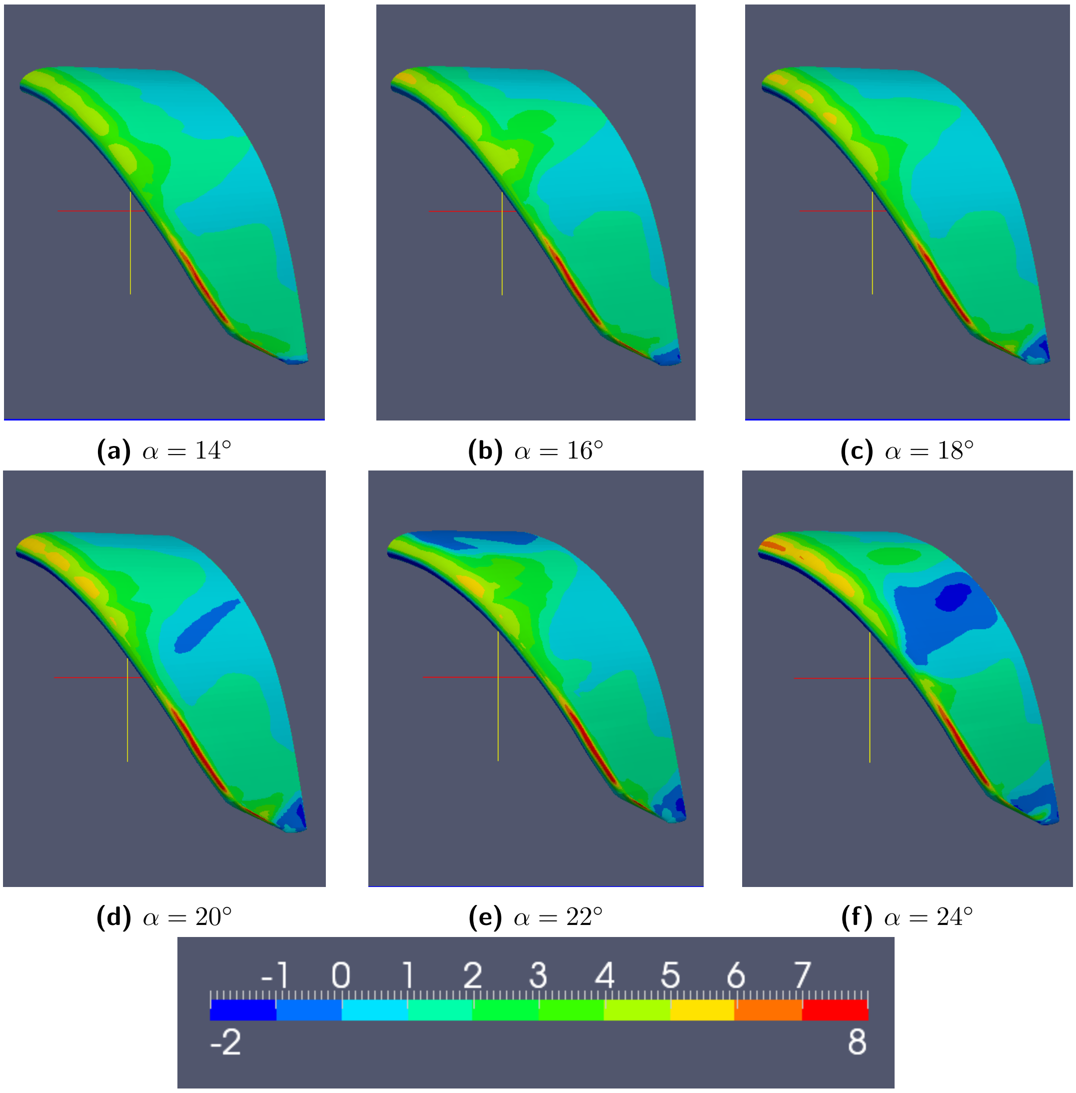

(a) $\alpha = 14°$ **(b)** $\alpha = 16°$ **(c)** $\alpha = 18°$

(d) $\alpha = 20°$ **(e)** $\alpha = 22°$ **(f)** $\alpha = 24°$

(g) Color legend, $\tau_{w,z}/\rho$ $[\mathrm{m}^3/\mathrm{s}^2]$

Figure 4.12: Flow separation off the suction surface. Negative values indicate regions of flow separation.

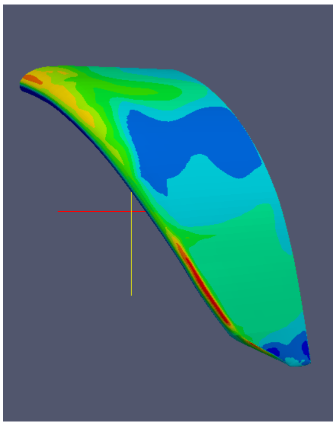

(a) $\alpha = 24°$, 8,000 iters.

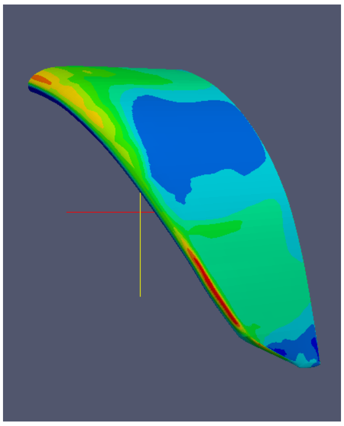

(b) $\alpha = 24°$, 10,000 iters.

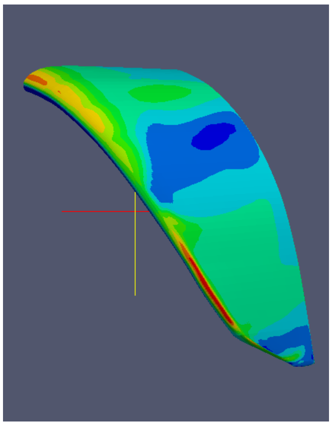

(c) $\alpha = 24°$, 16,000 iters.

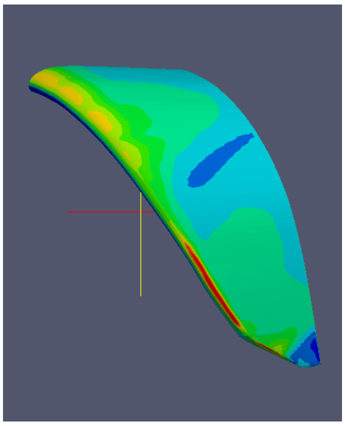

(d) $\alpha = 20°$, 24,000 iters.

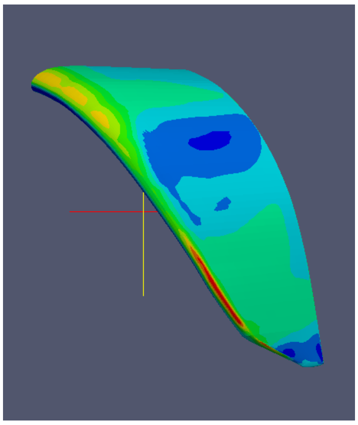

(e) $\alpha = 20°$, 28,000 iters.

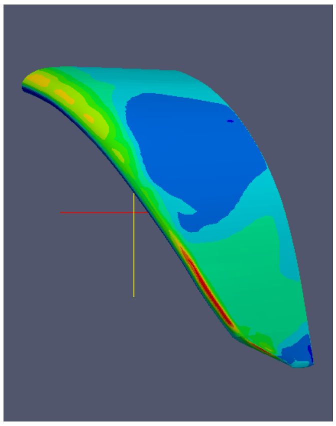

(f) $\alpha = 20°$, 30,000 iters.

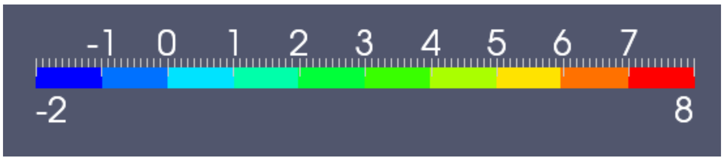

(g) Color legend, $\tau_{w,z}/\rho$ $[\mathrm{m}^3/\mathrm{s}^2]$

Figure 4.13: Changes in flow separation patterns as solution converges. Negative values indicate regions of flow separation.

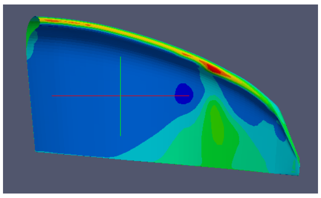

(a) $\alpha = -6°$

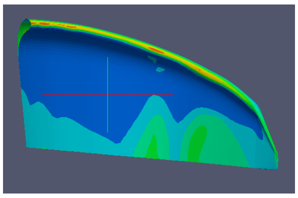

(b) $\alpha = -4°$

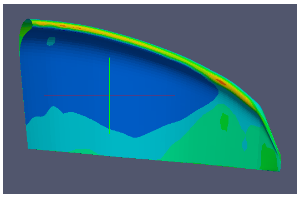

(c) $\alpha = -2°$

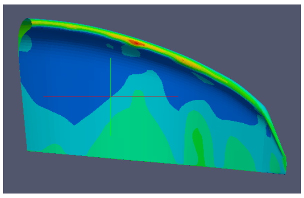

(d) $\alpha = 0°$

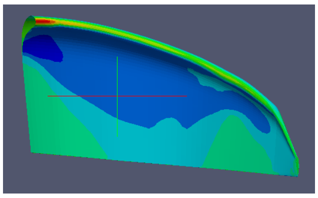

(e) $\alpha = 2°$

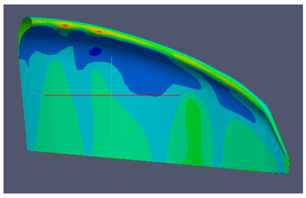

(f) $\alpha = 4°$

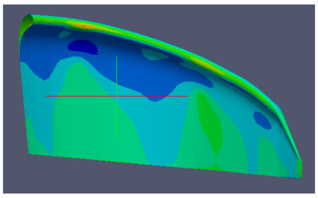

(g) $\alpha = 6°$

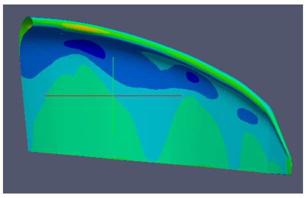

(h) $\alpha = 8°$

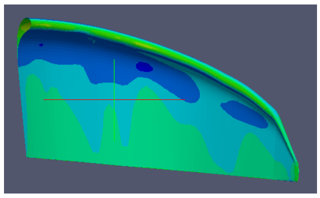

(i) $\alpha = 10°$

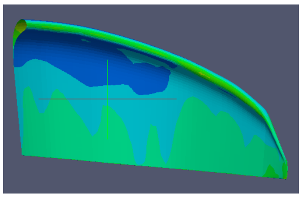

(j) $\alpha = 12°$

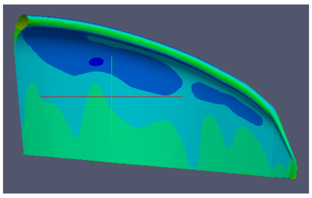

(k) $\alpha = 14°$

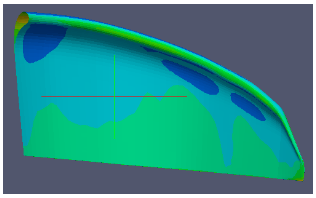

(l) $\alpha = 16°$

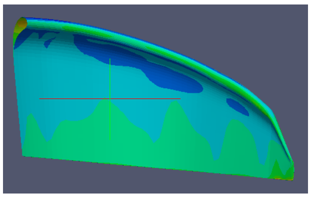

(m) $\alpha = 18°$

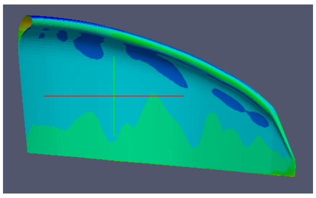

(n) $\alpha = 20°$

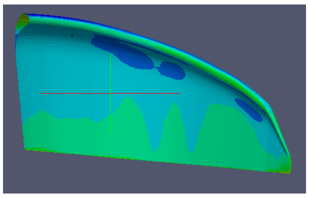

(o) $\alpha = 22°$

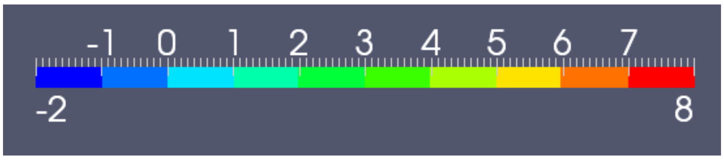

(p) Color legend, $\tau_{w,z}/\rho$ $[\mathrm{m}^3/\mathrm{s}^2]$

Figure 4.14: Flow separation behind the leading edge tube. Negative values indicate regions of flow separation.

Chapter 5

Discussion

5.1 Solution Convergence

Determining at which point the simpleFoam solver has reached a 'converged' solution is not as straight forward as it may seem. Two indicators are typically used to judge solution convergence.

Flow variable residuals are calculated by substituting the current flow solution into the equations and evaluating the difference between the left and right hand sides. The result is then normalized to be independent of the scale of the problem being solved. Flow variables below the level of 10^{-8} are a strong indication of solution convergence.

Since we are typically interested in the integral force coefficients, C_L & C_D, or C_x & C_y, monitoring these values directly is the second indicator of flow convergence. If the normalized changes in these coefficients between solution iterations is less than some prescribed tolerance, then the solution can said to be converged. A tolerance of 10^{-5} is a good starting point.

The difficulty comes because for many of the flows investigated the residuals never reach the level of 10^{-8} and the force coefficients never converge to one value. This is thought to be due to the unsteady nature of the separated flows that are investigated, as shown in subsection 4.3.7, and the steady state assumption used in the flow solver simpleFoam.

For the case of attached flow over the NACA0012 airfoil solution convergence was very quick and easy to determine from monitoring the force coefficients. As shown in Figure 5.1 the force coefficients converge within 1,000 iterations.

However for the case of the LEI kite the situation can be much more complicated, as shown in Figure 5.2. It appears that for this flow condition convergence similar to the NACA0012 $\alpha = 10°$ case is just not possible. It could be that if the solver was left to run for many more iterations that eventually a converged solution would be found, however resource limitations preclude this type of investigation. What is needed therefore is an engineering judgment that balances solution accuracy with computational expense.

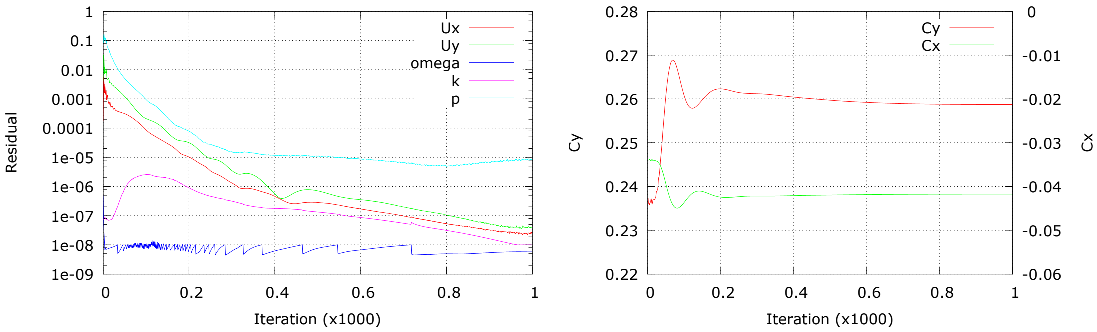

(a) Flow variable residuals. **(b)** Integral force coefficients.

Figure 5.1: simpleFoam solution convergence for NACA0012, $\alpha = 10°$

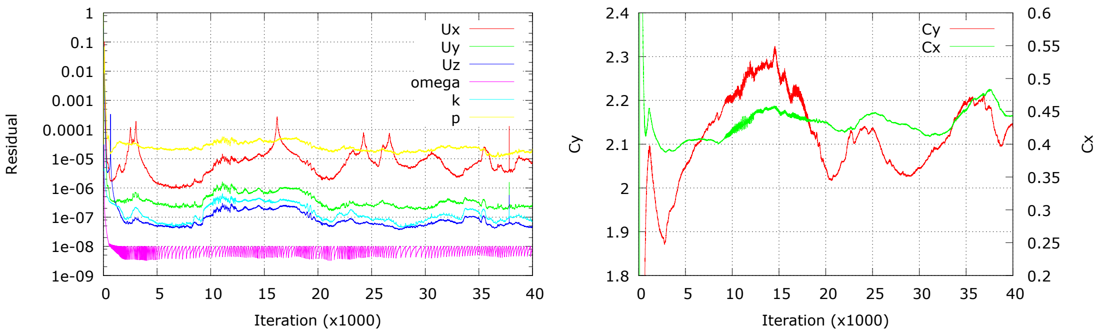

(a) Flow variable residuals. **(b)** Integral force coefficients.

Figure 5.2: simpleFoam solution convergence for V2 kite, $\alpha = 0°$

To further complicate matters the progress of the solution towards convergence is highly dependent on the mesh, solution settings, and flow conditions. What is deemed to be converged in one flow conditions is simply not possible to reach with another flow condition.

The solution convergence for all the results presented in this work can be found in Appendix A. In all cases the integral force coefficients reported were the average values of the final 500 iterations.

5.2 Computational Cost

It could be argued that reducing computational cost while maintaining solution accuracy is the main challenge for modern engineers, aerodynamicists in particular. Typically the level of accuracy achieved with a result is constrained by the computational resources available and the ingenuity of the engineering models used. Since resources are typically fixed, increasing solution accuracy requires more ingenious engineering solutions. Furthermore the value that can be created when coupling an aerodynamic model with a structural or optimization code can be very great, however this will require even further reductions in computational cost.

The RANS methods applied in this work are considered to be computationally expensive when compared to lower fidelity techniques. However this does not necessarily have to be the case. This section describes the costs of obtaining the results presented and discusses improvements that could be made to decrease these costs.

The extreme variation in computational costs between the 2D simulations of the NACA0012 airfoil and the 3D flow of the V2 kite cannot be understated. Shown in Table 5.1 is a comparison of these costs. It can be seen that the 3D simulations require over 400 times the processor hours. Discussed below are the number of factors that contribute to this severe increase in cost.

Table 5.1: Summary of computational costs.

Geometry	NACA0012	V2
Mesh cells	93,729	1.7 million
CPU	Intel®Core i5-2467M	AMD Opteron™Processor 6234
Cores	4	16
Core speed	1.6 GHz	2.4 GHz
nNonOrthogonal Correctors	0	4
Execution time per iteration	0.48 s	14.9 s
Approx. iterations needed	3,000	15,000
Total Time	24 min	62 hrs

5.2.1 nNonOrthogonalCorrectors

As discussed in subsection 3.3.2 the creation of the 3D mesh requires a hybrid approach due to the limitations of the hyperbolic mesh extrusion method when dealing with the large anhedral of the kite. Unfortunately this meshing technique tends to create very non-orthogonal cells at the boundary between the structured and unstructured mesh components. This causes severe solution instability unless a number of correction steps, called non-orthogonal correctors, are used to correct the pressure field for this effect. For the V2 kite solution stability was achieved with 4 non-orthogonal correctors. This means that the pressure correction step of the simpleFoam algorithm is performed 5 times. The pressure step is the most computationally expensive piece of the algorithm, requiring between 50 and 100 sub-iterations. Solving for the other flow variables typically needs less than 5 sub-iterations. The need to repeat the pressure correction step 4 more times therefore results in an almost 5 times increase in computational expense.

Removing these non-orthogonal cells could remove entirely the need for non-orthogoanl correctors and decrease computational costs substantially.

5.2.2 Number of Iterations Until Convergence

The number of iterations needed to reach solution convergence is influenced by a number of factors. Finite volume schemes used, the specifics of the flow, the mesh used, and the solution tolerances and relaxations factors all have an influence. For the 3D simulations of the V2 kite the number of iterations needed is typically larger than 10,000, while for the 2D simulations of the NACA0012 airfoil less than 5,000 were typically needed. This is obviously responsible for some of the large difference in computational cost between the two cases.

One way of decreasing the number of iterations needed to reach convergence is to initialize the flow domain with an already converged solution from a previously computed angle of attack. In OpenFOAM this can be accomplished by using the `mapFields` utility. For the case of the NACA0012 airfoil this utility worked great. Unfortunately with the large mesh of the V2 simulations the `mapFields` utility took hours to complete, offsetting any reduction in computational cost. It is still unknown whether this problem can be solved using different `mapFields` options, or if any other method could be used instead.

5.2.3 Mesh Size

The size of the mesh has an obvious effect on the computational cost. It was shown in subsection 4.3.1 that the mesh of size 186x63x80x40 was able to reproduce the results of a much finer mesh to within a few percent. The decrease in computation cost due to changes in mesh size was calculated on a per iteration basis using the three meshes presented in subsection 4.3.1. The metric of equivalent processor seconds per iteration was used to evaluate the difference in cost and is shown in Figure 5.3. The times shown were found for the Quad-Core AMD Opteron™8354 processor.

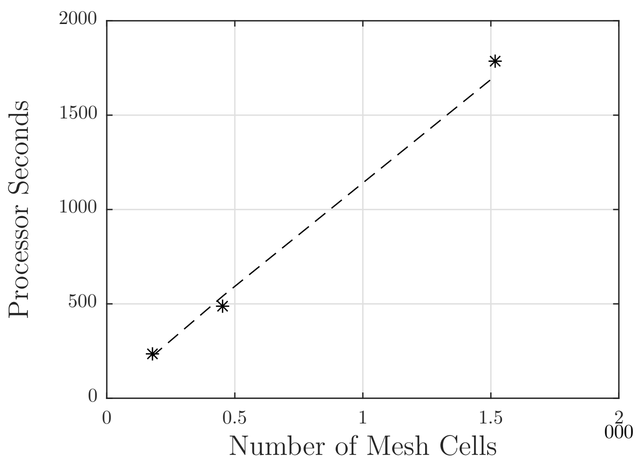

Figure 5.3: Computational cost of one simpleFoam solution iteration expressed in equivalent processor seconds.

A linear relationship between the number of mesh cells and the cost per iteration was found. This is considered to be very good performance and is indicative that the matirx solver chosen is performing well.

It is likely that by clustering cells in the areas of high flow gradients the number of mesh cells could be reduced without negatively impacting the solution accuracy. As shown this would have a linear effect on computational cost.

5.2.4 Multi-Grid Solvers

OpenFOAM comes with a number of different matrix solvers. The solvers used can be seen in Table 3.4. The multi-grid solvers available with OpenFOAM seek to reduce the number of iterations needed to reach convergence by first mapping the solution onto a coarser mesh, solving the flow equations, and then mapping that converged solution to the finer mesh before iterating further. This ensures that large scale flow features are resolved quickly on the coarse mesh first, increasing solution convergence. These matrix solvers were tried in the context of the V2 kite but for an unknown reason they caused large solution instability and hence could not be used. It is suspected that the hybrid mesh used is incompatible with the multi-grid solvers in OpenFOAM, but this is just speculation.

5.2.5 Commercial Software Packages

It is well known among the OpenFOAM community that when comparing OpenFOAM to many other commercially available flow solvers such as Star CCM or Fluent, that OpenFOAM is typically more sensitive to mesh quality, and is more unstable numerically. It could be the case that running identical simulations in a commercial package could negate the need for non-orthogonal correctors and require fewer solution iterations to reach convergence.

5.3 Kite Performance

As shown in Figure 4.11 the kite seems to perform optimally at an angle of attack somewhere between 14° and 20°. This is seen as very good news because if true it would mean that the kite is flying below stall conditions, perhaps allowing inviscid potential flow methods to accurately resolve the flow. However, this result does contradict the in flight data shown in Figure 2.3 which shows that the kite typically flies between 20° and 50° during the power production phase. Many explanations for this discrepancy are offered here.

The simplest explanation is perhaps that since the angle of attack information is not fed back to the ground station the kite is simply oriented incorrectly for maximum power production. This is relatively easy to check by adjusting the power lines during flight and recording the effect on tether traction.

Another explanation is that the data shown in Figure 4.11 is incorrect due to unsteady or FSI effects and that the kite actually can produce more lift than calculated at the higher angles of attack.

However the most likely cause of the discrepancy is the difficulty in determining accurately the chord line that was required to produce the results presented in Figure 2.3. Below is a direct quote from Ruppert's work that highlights this issue.

> It should be noticed that the angle of attack depends on the definition of the chord line. Currently the chord line is not defined and the measured angles

depend on the mounting of the X-Sense sensor. Consequently, the measured angles of attack will shift up or down depending on your chord line definition.

It is the opinion of the author that a 10° discrepancy in the definition of the chord line is present, and that the kite is flying at an average angle of near 20°, where it would be capable of producing the most power.

Chapter 6

Conclusions

The steady-state RANS solver simpleFoam, available from the open source CFD toolbox OpenFOAM, was used to evaluate the 3D viscous effects present in LEI kite flows. The meshing software Pointwise was used to mesh the kite. The following conclusions were reached.

Meshing

- Creating a fully structured mesh on the V2 is challenging due to the large anhedral of the kite. The hybrid meshing approach was found to be possible although at the expense of much larger computational costs.
- A mesh of approximately 1.7 million cells is capable of reproducing lift and drag results within a few percent of a much finer mesh.
- The geometric simplification of 'filling in' behind the leading edge tube has a negligible effect on the flow solution.
- Changing the size of the farfield boundary from 20 mid span chords to 80 mid span chords also has a negligible effect on the flow solution.

NACA0012

- The OpenFOAM solution under-predicts the lift by as much as 12% when compared to a number of experimental data sources.
- Simulation of the drag of a streamlined body such as the NACA0012 airfoil is very difficult. In general OpenFOAM over-predicts drag by somewhere between 5% and 78%, depending on the mesh and which experimental dataset is used for comparison.
- The pressure and skin friction distributions found from OpenFOAM match very well with the experimental data, meaning they are well suited for use in FSI simulations involving membrane flows.

V2 Flow Solution

- The SimpleFOAM solver is capable of producing reasonable results for the V2 kite at angles between $-6°$ and $24°$.
- At larger angles of attack SimpleFOAM becomes unstable and no solution could be found.
- Flow separation is seen to occur behind the leading edge tube at all angles studied. Separation from the suction surface begins to occurs between $18°$ and $20°$.
- Flow separation from the suction surface of the kite is responsible for the deviation from linear theory, mainly a decrease in lift and a large increase in drag, at angles of attack above $18°$.
- Flow separation from the suction side of the kite is seen to occur at the quarter span location before occurring at the mid span location.
- Flow separation from behind the leading edge tube at lower angles of attack, serves to decrease the effective camber of the kite, decreasing lift and increasing the lift curve slope.
- The V2 kite produces maximum cross-wind power at angles of attack between $14°$ and $20°$ depending on the parasitic drag of the tether and bridle lines.

Computational Cost and Solution Convergence

- Due to the large amount of flow separation determining solution convergence is only made possible by sound engineering judgment.
- The use of the hybrid meshing method introduces non-orthogonal cells which significantly increase the computational cost and may preclude the use of faster, less expensive multi-grid solvers.
- It is found that the computational cost is linearly related to the number of mesh cells.

Chapter 7

Recommendations

Based on the results presented a number of important recommendations can be made for future work.

Firstly the large computational costs can be seen as a direct consequence of the non-orthogonal cells present in the hybrid mesh. Techniques capable of building a fully structured, or fully unstructured mesh should be investigated. Also reductions in cell count from clustering or mesh refinement in certain key areas is likely to decrease computational costs further. Furthermore many mesh types are commonly used in CFD simulations other than the O-Mesh used here. Investigating these options is important to producing an optimum balance of solution accuracy and computational cost.

Significant geometric simplifications were made to the kite in order to make meshing easier. The inflated struts and bridle lines were removed and the tip geometry was modified slightly. The effect that these modifications have on the flow solution is at present unclear and should be investigated in future work.

A large amount of uncertainty still exists surrounding the apparent large discrepancy in drag found between the OpenFOAM simulations and experimental results. If the goal is to evaluate the kite's performance based on a metric involving the kite's drag this is seen as a significant problem. Questions that should be tackled include the laminar to turbulent transition of the boundary layer of the kite and the significance of pressure (form) drag vs. skin friction drag.

Despite the 'high fidelity' status granted to steady-state RANS solvers when compared to simpler inviscid methods, it would seem that steady-state RANS has quite a bit of trouble resolving the unsteady dynamics of flow separation. Solution convergence is difficult to achieve, and much engineering judgment has to be made regarding the results. Future researchers should perhaps investigate the use of unsteady flow solvers to deal with these issues. This however would first require significant improvements in computational efficiency since the costs of the steady-state solvers are already at the limit of what is possible with available resources.

Arguably one of the most significant simplifications made in this work is the assumption of a kite shape *a priori* from SurfPlan™, when in reality the kite shape in flight is determined by the much more complex FSI problem. Unfortunately unless significant improvements in computational efficiency are made the RANS methods described in this work are too computationally expensive to be used in an FSI setting. Therefore other methods of determining the kite shape in flight should be investigated. These methods could include photograph or video analysis, or simple bridle tension measurements coupled to a very simple kite structural model.

Finally the results presented in this work ignored a number of important flow factors that could prove to be significant in real LEI kite flows. Factors such as changes in Reynolds number, side slip angle and dynamic effects caused by changes in angle of attack or flow velocity have not been considered but are likely to be significant.

References

[1] Langley Research Center, Turbulence Modeling Resource, `http://turbmodels.larc.nasa.gov/naca0012_val.html`.

[2] I. Argatov, P. Rautakorpi, and R. Silvennoinen. Estimation of the mechanical energy output of the kite wind generator. *Renewable Energy*, 34(6):1525–1532, June 2009.

[3] Médéric Argentina and L. Mahadevan. Fluid-flow-induced flutter of a flag. *Proceedings of the National academy of Sciences of the United States of America*, 102.6:1829–1834, 2005.

[4] H Babinsky. Aerodynamic Improvements of Paraglider Performance. *American Institute of Aeronautics and Astronautics*, (99-3148), 1999.

[5] S. Banerjee and M. Patil. Aeroelastic analysis of membrane wings. *Proc. 49th AIAA/ASME/ASCE/AHS/ASC Structures, Structural Dynamics, and Materials Conference*, 2008.

[6] Julius Berens. *Advanced Fluid Structure Interactions Analysis of Flexible Membrane Wings*. Msc., Technische Universiteit Delft - Masters Thesis (In Progress), 2015.

[7] H A Bosch. *Finite element analysis of a kite for power generation.* Msc, Technische Universiteit Delft, 2012.

[8] Jeroen Breukels. *An Engineering Methodology for Kite Design.* Phd thesis, TU Delft, 2011.

[9] Pedro Carqueija. *Aerodynamic Investigations of a High-altitude Wind Energy Extraction System.* Msc, Riso/DTU - Universidade Tecnica de Lisboa - Msc. Thesis, 2010.

[10] Thomas Chatzikonstantinou. Recent advances in the numerical analysis of ram air wings - The three dimensional simulation code 'PARA3D'. In *RAeS/ AIAA 12th Aerodynamic Decelerator Systems Technology Conference*, page 11. AIAA, 1993.

[11] Thomas Chatzikonstantinou and Elek Puskas. Numerical Analysis of Three-Dimensional Non Rigid Wings. In *AIAA 10th Aerodynamic Decelerator Systems Conference*, page 20, Cocoa Beach, FL, 1989. AIAA.

[12] Antonello Cherubini, Andrea Papini, Rocco Vertechy, and Marco Fontana. Airborne Wind Energy Systems: A review of the technologies. *Renewable and Sustainable Energy Reviews*, 51:1461–1476, 2015.

[13] S. Collie, M. Gerritsen, and M. OâĂŹSullivan. Numerical Simulation of the turbulent flow past Upwind Yacht Sails. *Journal of Wind Engineering and Industrial Aerodynamics*, 91(2):185–197, 2002.

[14] George M. Dadd, Dominic A. Hudson, and R. Ajit Shenoi. Comparison of Two Kite Force Models with Experiment. *Journal of Aircraft*, 47(1):212–224, 2010.

[15] Aart de Wachter. *Deformation and Aerodynamic Performance of a Ram-air wing.* Msc, Technische Universiteit Delft, 2008.

[16] Moritz Diehl. Airborne Wind Energy: Basic Concepts and Physical Foundations. In *Airborne Wind Energy*, chapter 1, pages 3–22. Springer Berlin Heidelberg, Berlin, Heidelberg, 2013.

[17] Jeff D. Eldredge. Dynamically coupled fluidâĂŞbody interactions in vorticity-based numerical simulations. *Journal of Computational Physics*, 227(21):9170–9194, November 2008.

[18] Uwe Fechner and Roland Schmehl. Model-Based Efficiency Analysis of Wind Power Conversion by a Pumping Kite Power System. In Diehl; Ahrens; Schmehl;, editor, *Airborne Wind Energy*, chapter 14, pages 245–266. Springer Netherlands, 2013.

[19] Uwe Fechner, Rolf Van Der Vlugt, Edwin Schreuder, and Roland Schmehl. Dynamic Model of a Pumping Kite Power System. *submitted to Renewable Energy*, 2014.

[20] S.P. Fiddes and J.H. Gaydon. A new vortex lattice method for calculating the flow past yacht sails. *Journal of Wind Engineering and Industrial Aerodynamics*, 63(1-3):35–59, October 1996.

[21] J Furfaro and CE Haileyf. An experimental study of parafoil sections. 1997.

[22] Mac Gaunaa, Pedro Filipe Paralta Carqueija, Pierre-Elouan Réthoré, and Niels N. Sorensen. A computationally efficient method for determining the aerodynamic performance of kites for wind energy applications. In *EWEA 2011*, Brussels, 2011.

[23] K. Graf, A.v. Hoeve, and S. Watin. Comparison of full 3D-RANS simulations with 2D-RANS/lifting line method calculations for the flow analysis of rigid wings for high performance multihulls. In *3rd International Conference on Innovation in High Performance Sailing Yachts*, pages 71–84, Lorient, France, July 2013.

[24] S. Greenhalgh, H. C. Jr. Curtiss, and B. Smith. Aerodynamic properties of a two-dimensional inextensible flexible airfoil. *AIAA Journal*, 22(7):865–870, May 1984.

[25] N. Gregory and C.L. O'Reilly. Low-Speed Aerodynamic Characteristics of NACA 0012 Aerofoil Section, including the Effects of Upper-Surface Roughness Simulating Hoar Frost. *Reports and Memoranda*, 3726(3726):35, 1970.

[26] Sergio Hoyas and Javier Jiménez. Scaling of the velocity fluctuations in turbulent channels up to Reτ=2003. *Physics of Fluids*, 18, 2006.

[27] S.J. Hulshoff. CFD II Part 2: Computation and Modelling of Turbulence. TU Delft, 2012.

[28] Jeppe Johansen. Prediction of Laminar Turbulent Transition in Airfoil flows. *Riso National Laboratory, Roskilde, Denmark*, 36:731–734, 1999.

[29] J. Katz and A. Plotkin. *Low Speed Aerodynamics*. Cambridge University Press, Cambridge, UK, 2nd edition, 2010.

[30] A.N. Kolmogorov. Dissipation of Energy in the Locally Isotropic Turbulence. *Mathematical and Physical Sciences*, 434(1890), 1941.

[31] A.N. Kolmogorov. The Local Structure of Turbulence in Incompressible Viscous Fluid for Very Large Reynolds Numbers. *Mathematical and Physical Sciences*, 434(1890), 1941.

[32] Charles L. Ladson. Effects of independent variation of Mach and Reynolds numbers on the low-speed aerodynamic characteristics of the NACA 0012 airfoil section. 1988.

[33] B.E. Launder and D.B. Spalding. The numerical computation of turbulent flows. *Computer Methods in Applied Mechanics and Engineering*, 3:269–289, 1974.

[34] O. Le Maître, S. Huberson, and E. Souza De Cursi. Unsteady Model of Sail and Flow Interaction. *Journal of Fluids and Structures*, 13:37–59, 1999.

[35] Rachel Leuthold. Multiple-Wake Vortex Lattice Method for Airborne Wind Energy Membrane-Wing Kites. Technical report, 2015.

[36] O. Lorillu, R. Weber, and J. Hureau. Numerical and experimental analysis of two-dimensional separated flows over a flexible sail. *Journal of Fluid Mechanics*, 466:319–341, September 2002.

[37] ML Loyd. Crosswind kite power. *Journal of Energy*, (December 2007), 1980.

[38] Maneia. Aerodynamic study of airfoils and wings for power kites applications. Technical report, Delft University of Technology - Masters Thesis, 2007.

[39] Santiago Márquez Damián. An Extended Mixture Model for the Simultaneous Treatment of Short and Long Scale Interfaces. page 190, 2013.

[40] W. J. Mccroskey. A critical assessment of wind tunnel results for the NACA 0012 airfoil. 1987.

[41] M.R. Mendenhall, J. N. Nielsen, and S.B. Spangler. Review of methods for predicting the aerodynamic characteristics of parawings. *Journal of Aircraft*, 1968.

[42] FR Menter. Improved two-equation k-omega turbulence models for aerodynamic flows. *NASA STI/Recon Technical Report N*, 1992.

[43] J. N. Nielsen. Theory of Flexible Aerodynamic Surfaces. *Journal of Applied Mechanics*, 30(3):435, September 1963.

[44] S.V Patankar and D.B Spalding. A calculation procedure for heat, mass and momentum transfer in three-dimensional parabolic flows. *International Journal of Heat and Mass Transfer*, 15(10):1787–1806, 1972.

[45] M B Ruppert. *Development and validation of a real time pumping kite model.* Msc, Technische Universiteit Delft, 2012.

[46] A. M. O. Smith. Transition, Pressure Gradient, and Stability Theory. In *Proceedings IX International Congress of Applied Mechanics*, pages 234–244, 1956.

[47] Richard W. Smith. *A viscous flow based membrane wing model.* Phd, University of Florida, 1994.

[48] Rick Smith and Wei Shyy. Computation of aerodynamic coefficients for a flexible membrane airfoil in turbulent flow: A comparison with classical theory. *Physics of Fluids*, 8(12):3346, December 1996.

[49] P R Spalart and S R Allmaras. A one-equation turbulence model for aerodynamic flows. *La Recherche Aerospatiale*, 1:5–21, 1994.

[50] B. Thwaites. The Aerodynamic Theory of Sails. I. Two-Dimensional Sails. *Proceedings of the Royal Society A: Mathematical, Physical and Engineering Sciences*, 261(1306):402–422, May 1961.

[51] J.L. van Ingen. A suggested semi-empirical method for the calculation of the boundary layer transition region. 1956.

[52] R. H. M Van Kappel. *Aerodynamic analysis tool for dynamic leading edge inflated kite models: a nonlinear vortex lattice method.* Msc, Technische Universiteit Delft, 2012.

[53] H.K. Versteeg and W Malalasekera. *Introduction to Computational Fluid Dynamics.* Pearson Education Ltd., 2nd edition, 2005.

[54] I. M. Viola, P. Bot, and M. Riotte. Upwind sail aerodynamics: A RANS numerical investigation validated with wind tunnel pressure measurements. *International Journal of Heat and Fluid Flow*, 39:90–101, 2013.

[55] K. Voelz. Profil und Auftrieb eines Segels. *Math. Mech.*, 30:301–317, 1950.

[56] Frank M White. Viscous Fluid Flow. *New York*, Second:413, 2000.

[57] Shun C. Yen and Yu F. Fei. Winglet Dihedral Effect on Flow Behavior and Aerodynamic Performance of NACA0012 Wings. *Journal of Fluids Engineering*, 133(7):071302, 2011.

Appendix A

3D V2 Solution Convergence

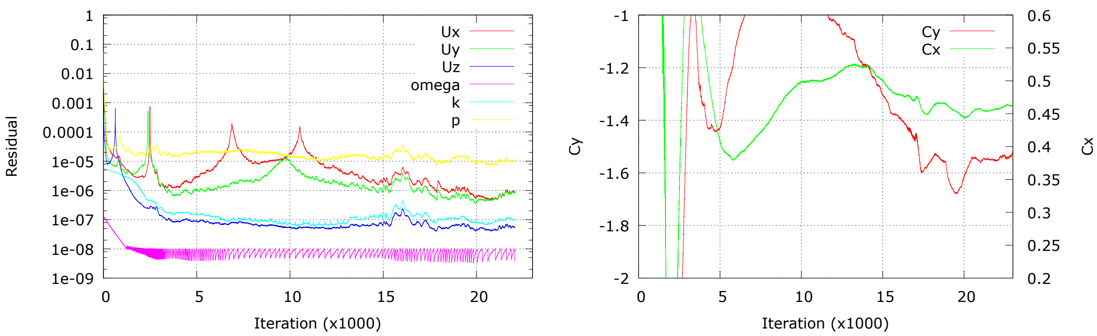

(a) Flow variable residuals. **(b)** Integral force coefficients.

Figure A.1: SimpleFOAM solution convergence, $\alpha = -6°$, 186x63x80x60.

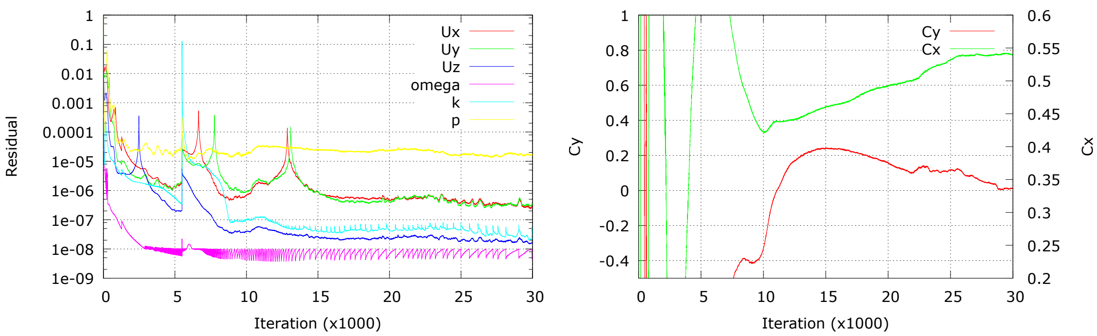

(a) Flow variable residuals. **(b)** Integral force coefficients.

Figure A.2: SimpleFOAM solution convergence, $\alpha = -4°$, 186x63x80x60.

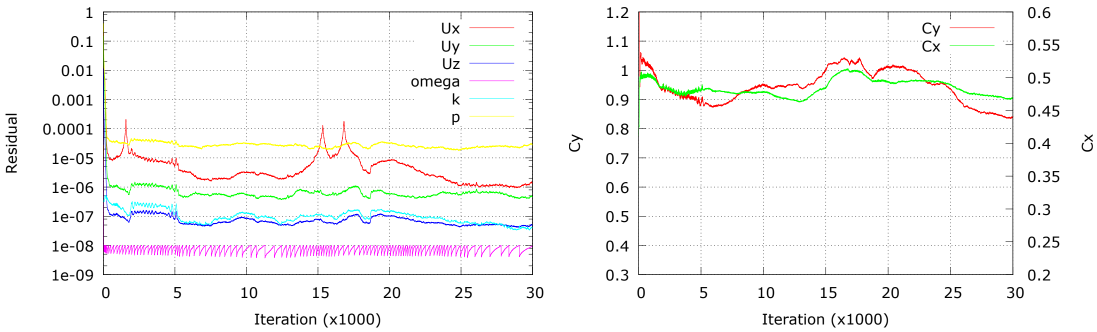

(a) Flow variable residuals. **(b)** Integral force coefficients.

Figure A.3: SimpleFOAM solution convergence, $\alpha = -2°$, 186x63x80x60.

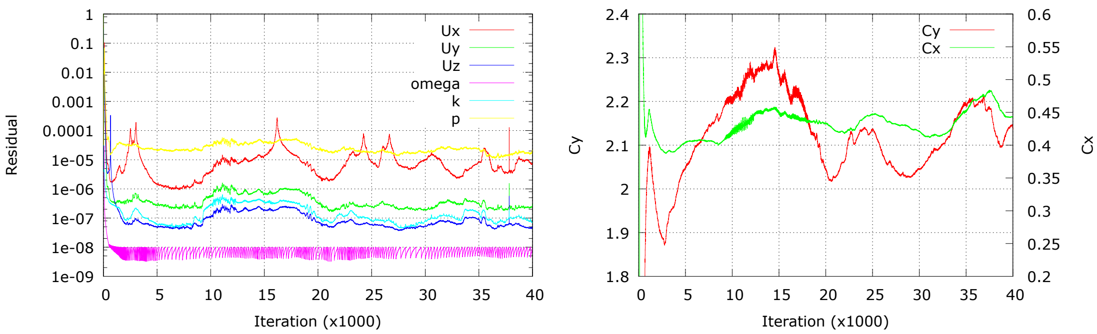

(a) Flow variable residuals. **(b)** Integral force coefficients.

Figure A.4: SimpleFOAM solution convergence, $\alpha = 0°$, 186x63x80x60.

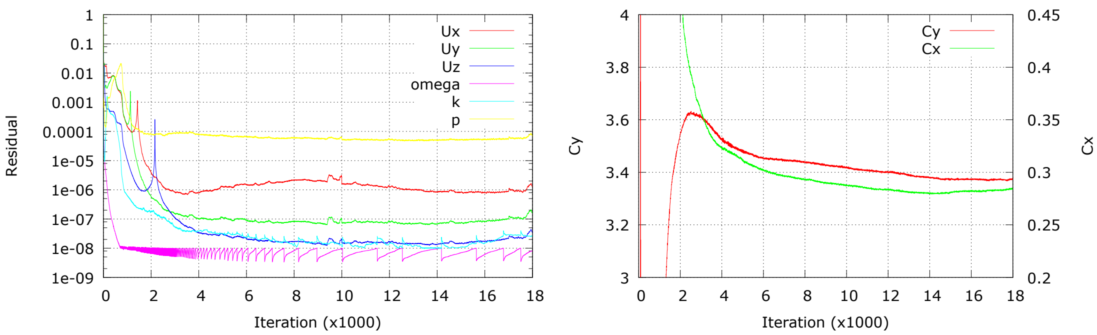

(a) Flow variable residuals. **(b)** Integral force coefficients.

Figure A.5: SimpleFOAM solution convergence, $\alpha = 2°$, 186x63x80x60.

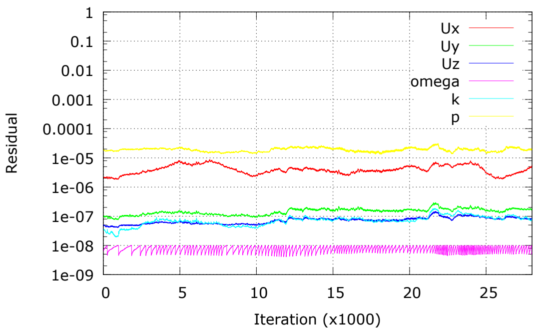

(a) Flow variable residuals.

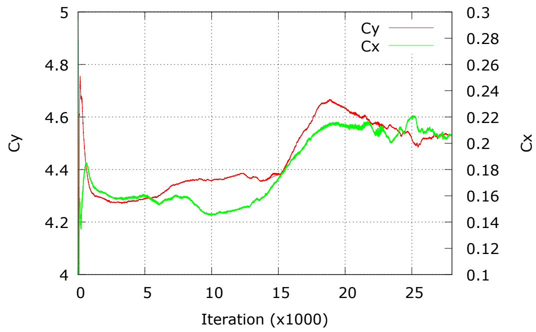

(b) Integral force coefficients.

Figure A.6: SimpleFOAM solution convergence, $\alpha = 4°$, 186x63x80x60.

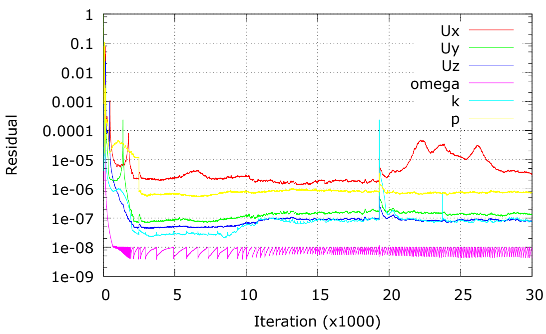

(a) Flow variable residuals.

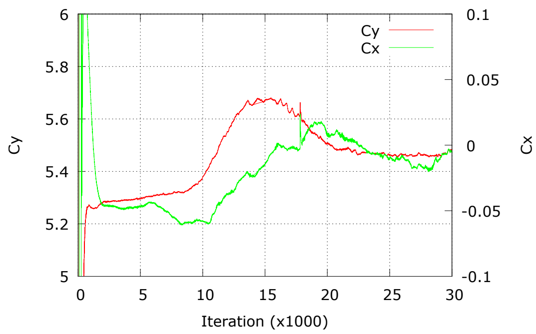

(b) Integral force coefficients.

Figure A.7: SimpleFOAM solution convergence, $\alpha = 6°$, 186x63x80x60.

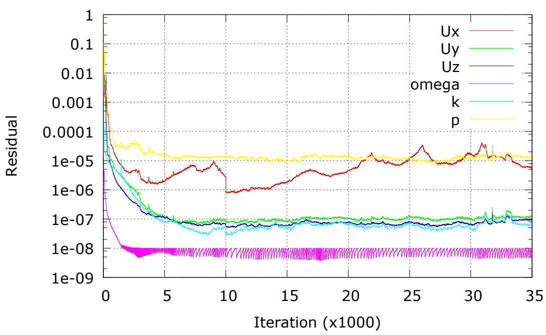

(a) Flow variable residuals.

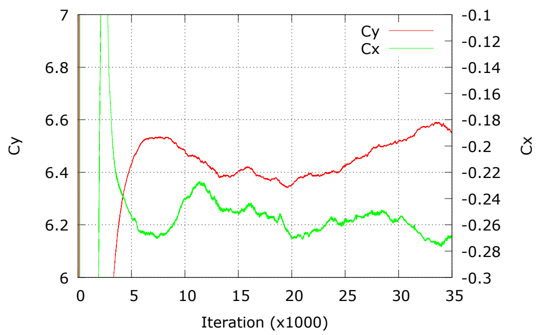

(b) Integral force coefficients.

Figure A.8: SimpleFOAM solution convergence, $\alpha = 8°$, 186x63x80x60.

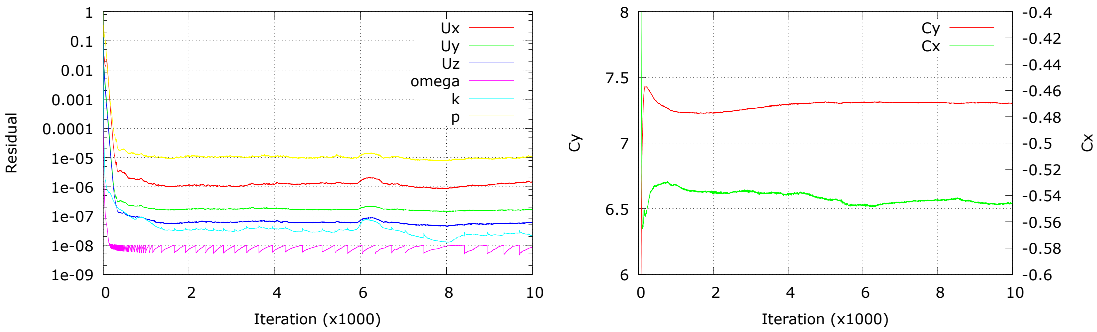

(a) Flow variable residuals. **(b)** Integral force coefficients.

Figure A.9: SimpleFOAM solution convergence, $\alpha = 10°$, 186x63x80x60.

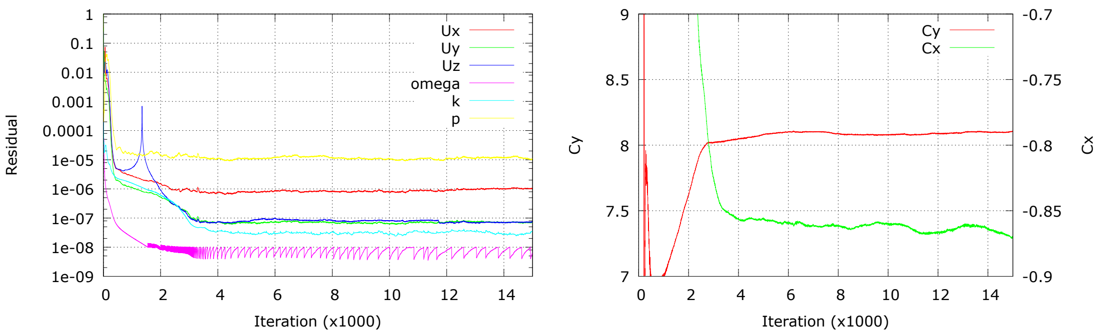

(a) Flow variable residuals. **(b)** Integral force coefficients.

Figure A.10: SimpleFOAM solution convergence, $\alpha = 12°$, 186x63x80x60.

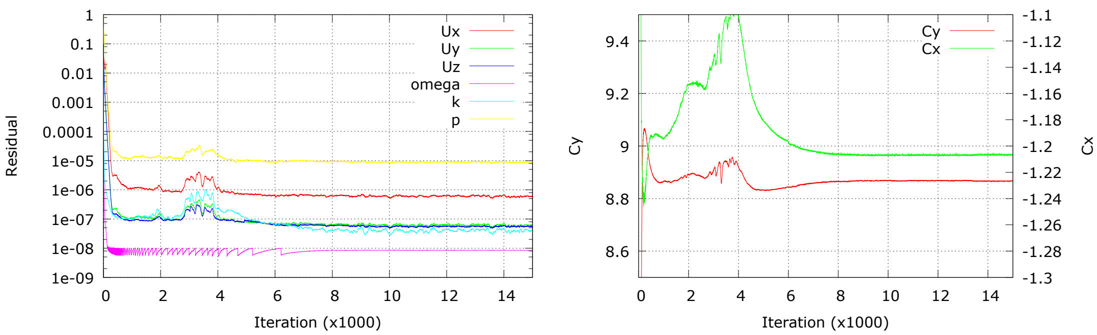

(a) Flow variable residuals. **(b)** Integral force coefficients.

Figure A.11: SimpleFOAM solution convergence, $\alpha = 14°$, 186x63x80x60.

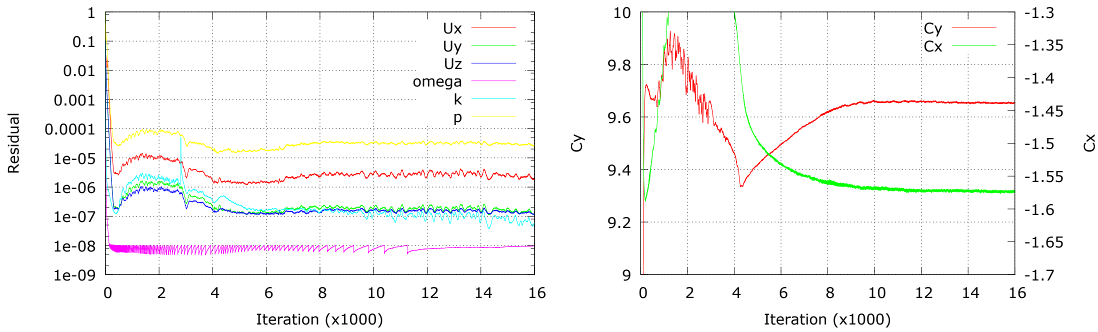

(a) Flow variable residuals. **(b)** Integral force coefficients.

Figure A.12: SimpleFOAM solution convergence, $\alpha = 16°$, 186x63x80x60.

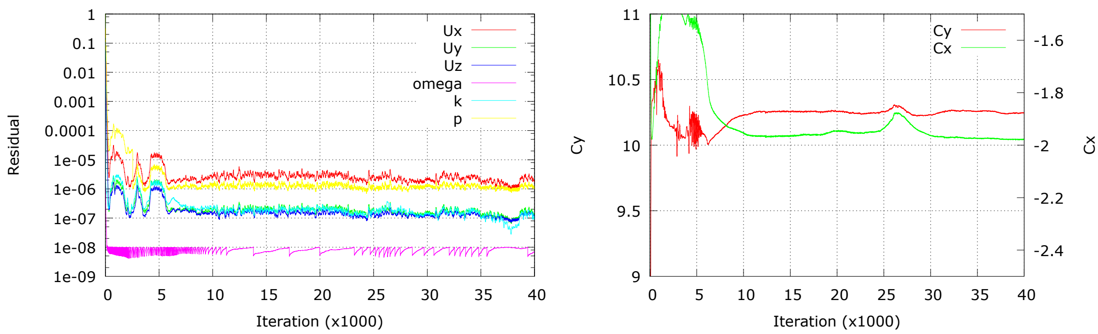

(a) Flow variable residuals. **(b)** Integral force coefficients.

Figure A.13: SimpleFOAM solution convergence, $\alpha = 18°$, 186x63x80x60.

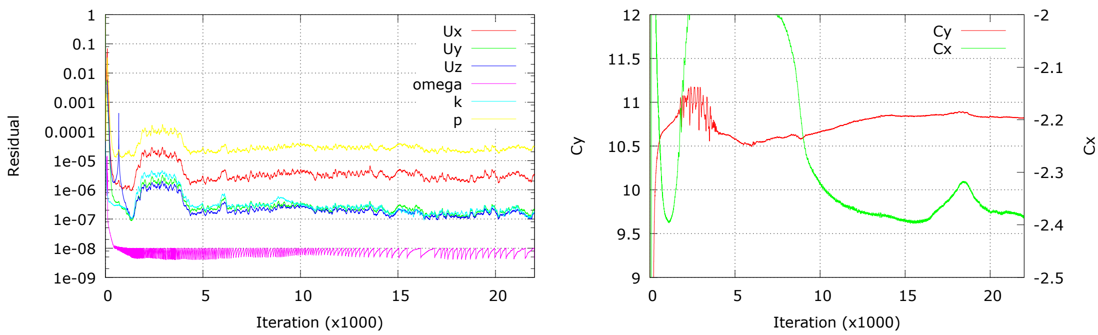

(a) Flow variable residuals. **(b)** Integral force coefficients.

Figure A.14: SimpleFOAM solution convergence, $\alpha = 20°$, 186x63x80x60.

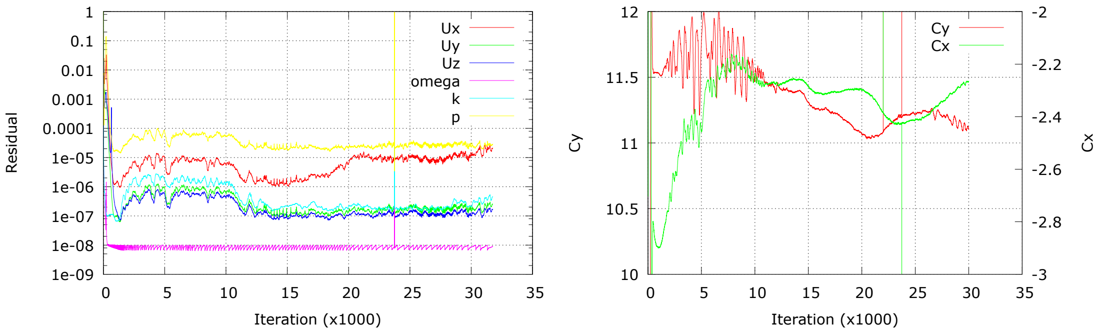

(a) Flow variable residuals. **(b)** Integral force coefficients.

Figure A.15: SimpleFOAM solution convergence, $\alpha = 22°$, 186x63x80x60.

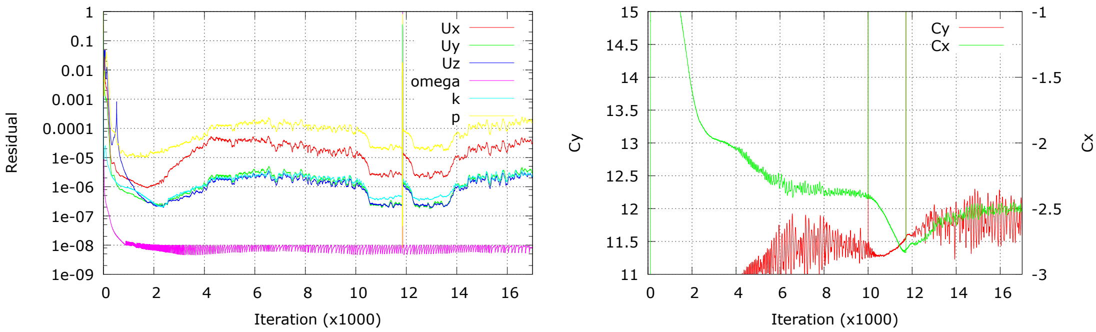

(a) Flow variable residuals. **(b)** Integral force coefficients.

Figure A.16: SimpleFOAM solution convergence, $\alpha = 24°$, 186x63x80x60.

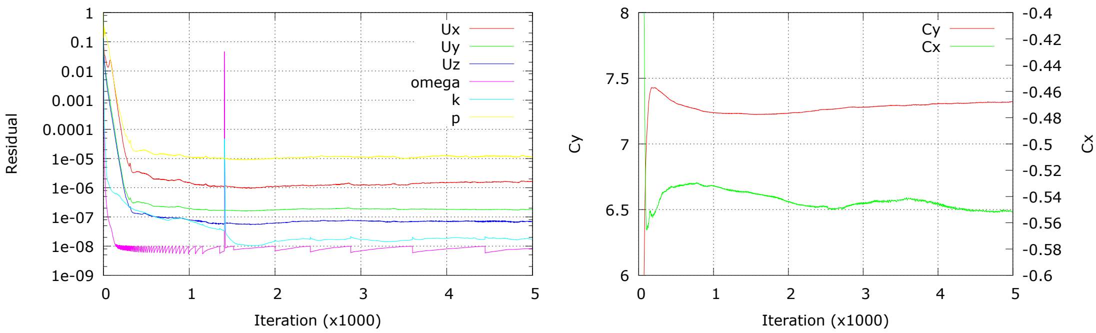

(a) Flow variable residuals. **(b)** Integral force coefficients.

Figure A.17: SimpleFOAM solution convergence, $\alpha = 10°$, 186x63x80x60, high turbulence boundary condition.

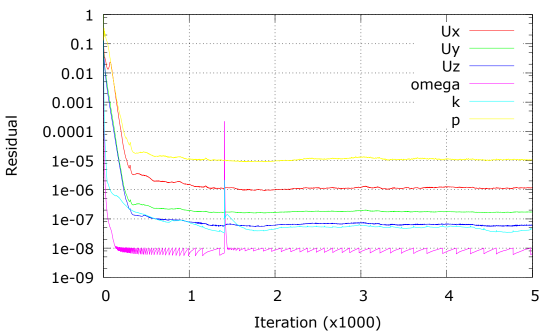

(a) Flow variable residuals.

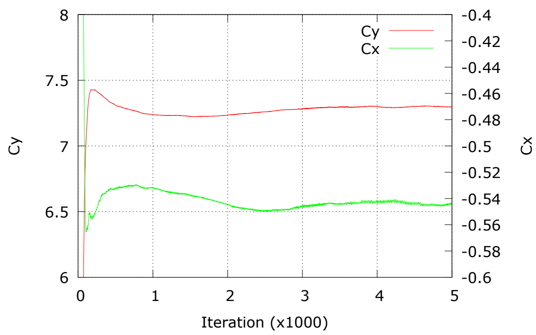

(b) Integral force coefficients.

Figure A.18: SimpleFOAM solution convergence, $\alpha = 10°$, 186x63x80x60, low turbulence boundary condition.